IRAQI JOURNAL OF APPLIED PHYSICS

The *Iraqi Journal of Applied Physics (IJAP)* is a peer reviewed journal of high quality devoted to the publication of original research papers from applied physics and their broad range of applications. IJAP publishes quality original research papers, comprehensive review articles, survey articles, book reviews, dissertation abstracts in physics and its applications in the broadest sense. It is intended that the journal may act as an interdisciplinary forum for Physics and its applications. Innovative applications and material that brings together diverse areas of Physics are particularly welcome. Review articles in selected areas are published from time to time. It aims to disseminate knowledge; provide a learned reference in the field; and establish channels of communication between academic and research experts, policy makers and executives in industry, commerce and investment institutions. IJAP is a quarterly specialized periodical dedicated to publishing original papers, letters and reviews in: Applied & Nonlinear Optics, Applied Mechanics & Thermodynamics, Digital & Optical Communications, Electronic Materials & Devices, Laser Physics & Applications, Plasma Physics & Applications, Quantum Physics & Spectroscopy, Semiconductors & Optoelectronics, and Solid State Physics & Applications

SPONSORED AND PUBLISHED BY
THE IRAQI SOCIETY FOR ALTERNATIVE AND RENEWABLE ENERGY SOURCES & TECHNIQUES (I.S.A.R.E.S.T.)

IRAQI JOURNAL OF APPLIED PHYSICS
" INSTRUCTIONS TO AUTHORS "

CONTRIBUTIONS

Contributions to be published in this journal should be original research works, i.e., those not already published or submitted for publication elsewhere, individual papers or letters to editor.

SUBMISSION OF MANUSCRIPTS

Manuscripts should be submitted to the editor at the mailing address:

Iraqi Journal of Applied Physics
Editorial Board
P. O. Box 55259, Baghdad 12001, IRAQ, submission@ijap.org , editor@ijap.org

MANUSCRIPTS

Two hard copies with soft copy on a compact disc (CD) should be submitted to Editor in the following configuration:

- Double-spaced one-side A4 size with 2.5 cm margins of all sides
- Times New Roman font (16pt bold for title, 14pt bold for names, 12pt bold for headings, 12pt regular for text)
- Letters should not exceed 10 pages, papers should not exceed 20 pages and reviews are up to author.
- Manuscripts presented in English only are accepted.
- English abstract not exceed 150 words
- 4 keywords (at least) should be maintained on (PACS preferred)
- Author(s) should express all quantities in SI units
- Equations should be written in equation form (*italic* and symbolic)
- Figures and Tables should be separated from text
- Figures and diagrams can be submitted in colors for assessment and they will be returned to authors after provide printable copies
- Charts should be indicated by the software used for
- Only original or high-resolution scanner photos are accepted
- For electronic submission, articles should be formatted with MS-Word software.

AUTHOR NAMES AND AFFILIATIONS

It is IJAP policy that all those who have participated significantly in the technical aspects of a paper be recognized as co-authors or cited in the acknowledgments. In the case of a paper with more than one author, correspondence concerning the paper will be sent to the first author unless staff is advised otherwise.

Author name should consist of first name, middle initial, last name. The author affiliation should consist of the following, as applicable, in the order noted:

- Company or college (with department name or company division)
- Postal address
- City, state, zip code
- Country name
- Telephone, and e-mail

REFERENCES

The references should be brought at the end of the article, and numbered in the order of their appearance in the paper. The reference list should be cited in accordance with the following examples:

[1] X. Ning and M.R. Lovell, "On the Sliding Friction Characteristics of Unidirectional Continuous FRP Composites", *ASME J. Tribol.*, 124(1) (2002) 5-13.
[2] M. Barnes, "Stresses in Solenoids", *J. Appl. Phys.*, 48(5) (2001) 2000–2008.
[3] J. Jones, "Contact Mechanics", Cambridge University Press (Cambridge, UK) (2000), Ch.6, p.56.
[4] Y. Lee, S.A. Korpela and R. Horne, "Structure of Multi-Cellular Natural Convection in a Tall Vertical Annulus", Proc. 7th International Heat Transfer Conference, U. Grigul et al., eds., Hemisphere (Washington DC), 2 (1982) 221–226.
[5] M. Hashish, "Waterjet Technology Development", High Pressure Technology, PVP-Vol. 406 (2000), 135-140.
[6] D.W. Watson, "Thermodynamic Analysis", ASME Paper No. 97-GT-288 (1997).
[7] C.Y. Tung, "Evaporative Heat Transfer in the Contact Line of a Mixture", Ph.D. thesis, Rensselaer Polytechnic Institute, Troy, NY (1982).

PROOFS

Authors will receive proofs of papers and are requested to return one corrected hard copy with a WORD copy on a compact disc (CD). New materials inserted in the original text without Editor permission may cause rejection of paper.

COPYRIGHT FORM

Author(s) will be asked to transfer copyrights of the article to the Journal soon after acceptance of it. This will ensure the widest possible dissemination of information.

OFFPRINTS

Authors will receive offprints free of charge and any additional offprints can be ordered.

SUBSCRIPTION AND ORDERS

Annual fees (4 issues per year) of subscription are:

- 50 US$ for individuals inside Iraq.
- 100 US$ for establishments inside Iraq.
- 100 US$ for individuals abroad.
- 200 US$ for establishments abroad.

Fees are reduced by 25% for I.S.A.R.E.S.T. members. Orders of issues can be submitted by contacting the editor-in-chief or editorial office at **subscription@ijap.org** to maintain the address of issue delivery and payment way.

A New Miniature Narrowband Microstrip Bandpass Filter Design Based on Peano Fractal Geometry

Jawad K. Ali
Yaqeen S. Mezaal

Department of Electrical & Electronic Engineering, University of Technology P. O. Box 35239, Baghdad, Iraq

A new compact narrowband multiresonator microstrip filter design is presented in this paper as a candidate for use in modern wireless communication systems. The proposed filter structure is generated using Peano fractal curve geometry. The proposed filter structure is fractally generated using Peano fractal curve geometry. Two 2nd and 4th order Chebyshev bandpass filters have been designed based on the 2nd iteration Peano fractal curve at a design frequency of 2.45GHz using a substrate of a relative dielectric constant of 9.6 and thickness of 0.508 mm. Filter structures based on the second iteration Peano geometry leads to compact size single mode resonators with dimensions of about (0.075×0.086)λ_g. This article represents better miniaturization level compared with the other microstrip bandpass filters based on other space-filling geometries and designed at the same frequency using the same substrate material specifications. Simulation and theoretical performance of the resulting filter structures have been carried out using method of moments (MoM) based electromagnetic simulator IE3D, from Zeland Software Inc. The results also show that the proposed filter structures possess good return loss and transmission responses besides the size reduction gained, making them suitable for use in a wide variety of wireless communication applications.

Keywords: Fractal single mode resonator, Bandpass filter, Narrow-band microstrip filter, Peano fractal geometry
Received: 10 September 2009, **Revised**: 30 September 2009, **Accepted**: 7 October 2009

1. Introduction

A wide variety of applications for fractal has been found in many areas of science and engineering, since the pioneer work of Mandelbrot [1]. One such area is fractal electrodynamics [2] in which fractal geometry is combined with electromagnetic theory for the purpose of investigating a new class of radiation, propagation, and scattering problems. One of the most promising areas of fractal electrodynamics research is its application to the antenna and microwave circuits design.

Fractals represent a class of geometries with very unique properties that can be attractive for microwave circuit designers. Fractal space filling contours, meaning electrically large features can be efficiently packed into small area. Since the electrical lengths play such an important role in microwave circuit design, this efficient packing can be used as viable miniaturization technique. The space filling properties lead to curves that are electrically very long, but fit into a compact physical space. This property can lead to the miniaturization of antenna elements.

Among the earliest predictions of the use of fractals in the design and fabrication of filters is that of Yordanov *et al.,* [3]. Their predictions are based on their investigation of Cantor fractal geometry. Hilbert fractal curve has been used as a defected ground structure in the design of a microstrip lowpass filter operating at the L-band microwave frequency [4]. Based on this fractal curve, compact high temperature superconductor microstrip bandpass resonator filters have been designed for wireless communication applications [5,6]. Sierpinski fractal geometry has been used in the implementation of a complementary split ring resonator [7]. Split ring geometry using square Sierpinski fractal curves has been proposed to reduce resonant frequency of the structure and to achieve improved frequency selectivity in the resonator performance.

Koch fractal shape is applied to mm-wave microstrip bandpass filters integrated on a high-resistivity substrate [8]. Results showed that the 2nd harmonic of fractal shape filters can be suppressed as the fractal factor increases, while maintaining the physical size of the resulting filter design [9]. Recently, a modified configuration of Minkowski-island and Koch fractal curves have been used to design

miniaturized microstrip dual-mode bandpass filters for mobile applications [10,11]. It is worth to note here, that most of the previously mentioned fractal geometries have been first applied to design compact size multiband antennas.

In this paper, a novel narrowband multi-resonator microstrip filter design has been presented for use in the modern compact communication systems. Based on the 2nd iteration Peano fractal curve geometry, a 4-pole Chebyshev bandpass resonator filter has been designed at 2.45GHz with fractional bandwidth of 10%. The resulting filter has been found to possess a considerable miniaturization owing to its remarkable space filling property together with good transmission and return loss responses. The design strategy adopted in this work is that developed by Swanson [12]. Swanson combined the concepts of Dishal [13], the EM simulation, and the port tuning method to outline a general and powerful procedure for a narrowband multi-resonator filter design. Dishal's design method for narrowband filters offers a very simple and intuitive approach that can be applied to different filter technologies and topologies. It makes use of measured experimental hardware to generate two design curves. Based on these design curves, a complete Chebyshev bandpass multiresonator filter structure with the required order and specifications can be obtained in a very efficient and potentially more accurate way, compared with the previous experimental method [12].

2. The Peano Fractal Curve

It is noteworthy that the Peano curve, proposed by Peano in 1890, was, in fact, the first set of space-filling curve [14]. One interesting feature of the Peano-curve algorithm is its relatively higher compression rate than the Hilbert-curve algorithm in filling a 2-D region, which suggests that the Peano resonator may resonate at a lower fundamental resonant frequency than a comparable Hilbert resonator of the same iteration order k. The Peano fractal curve, as shown in Fig. (1), consists in a continuous line which connects the centers of a uniform background grid. The fractal curve is fit in a square section of S as external side. By increasing the iteration level k of the curve, one reduces the elemental grid size as $S/(3^k\text{-}1)$; the space between lines diminishes in the same proportion. For a Peano resonator, made of a thin conducting strip in the form of the Peano curve with side dimension S and order k, the length of each line segment d and the sum of all the line segments $L(k)$ are given by [15]

$$L(k) = (3^k + 1)S \qquad (1)$$

The main idea here is to increase the iteration of the Peano curve as much as possible in order to fit the resonator in the smallest area. However, it has been found that, when dealing with space-filling fractal shaped microstrip resonators, there is a tradeoff between miniaturization (curves with high k) and quality factor of the resonator. For a microstrip resonator, the width of the strip w and the spacing between the strips g are the parameters which actually define this tradeoff [6]. Both dimensions (w and g) are connected with the external side S and iteration level k ($k \geq 2$) by

$$S = 3^k (w + g) - g \qquad (2)$$

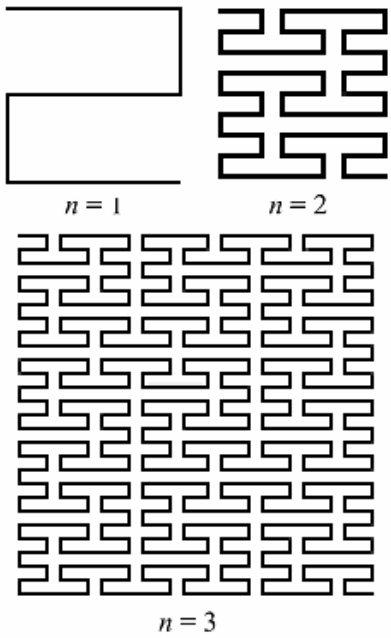

Fig. (1) The first three iteration levels of the Peano fractal curve generation process

From this equation, it is clear that trying to obtain higher levels of fractal iterations; this will lead to lower values of the microstrip width, thus increasing the dissipative losses with a corresponding degradation of the resonator quality factor. Hence, for these structures, the compromise between miniaturization and quality factor is simply defined by an adequate fractal iteration level. However, it has been concluded, in practice, that the number of generating iterations required to reap the benefits of miniaturization is only few before the additional complexities become indistinguishable [16].

The dimension of a fractal provides a description of how much a space it fills [17]. It is a measure of the prominence of the irregularities when viewed at very small scales. A dimension contains much information about the geometrical properties of a fractal. Because the total length of the conducting strip is larger than that of the same order Hilbert resonator, which is $(2^k+1)S$, it would be expected that the Peano

resonator resonates at a lower fundamental frequency than the same order Hilbert resonator [18].

3. The Proposed Filter Design

A bandpass filter specification generally includes the desired center frequency, bandwidth, maximum insertion loss in the passband, and several required rejection levels in the stopbands. There will also be a specification on the minimum return loss in the passband. Many mechanical filters with tuning screws can eventually be tuned to their designed return loss level. In planar filters, which are much harder to tune, one might design for -20dB return loss and hopes to achieve a minimum of -15dB in previous work [12]. Once the prototype ripple level has been determined, the filter order N can be estimated based on the desired stopband rejection. The graphs and equations in [19] are very useful for estimating filter order. It should be noted that the graphs and equations assume an ideal, symmetrical Chebyshev response. Some microwave filters have symmetrical stopband responses, so the required order may be higher or lower than what is originally estimated. With the ripple level and order N determined, the tables or equations can be used to find the normalized lowpass prototype values. Table (1) lists the normalized element values for a 0.036 dB ripple, Chebyshev lowpass prototype. The midband filter loss can be estimated using the expected average unloaded Q for the resonators [12,20]:

$$Loss(f_o) = \frac{4.343 f_o}{\Delta f Q_u} \sum_{i=1}^{N} g_1(dB) \qquad (3)$$

where Δf is the equal ripple bandwidth of the filter and the sum of the g_is can be found in the last column of Table (1). Equation (3) can also be rearranged to predict the required unloaded Q given a desired midband insertion loss. Unloaded Q is proportional to a dominant resonator dimension and can be sensitive to manufacturing processes as well. Insertion loss in the passband is also proportional to time delay and will increase at the band edges.

Table (1) Chebyshev lowpass prototype for 0.036dB Ripple, 20.8dB Return Loss [19]

N	g_0	g_1	g_2	g_3	g_4	g_5	g_6	g_7	g_8	g_9	g_{10}	$\sum_{i=1}^{N} g_i$
2	1.0000	0.6323	0.5269	1.1999								1.1592
3	1.0000	0.8185	1.0895	0.8185	1.0000							2.7265
4	1.0000	0.8989	1.2843	1.5410	0.7491	1.1999						4.4733
5	1.0000	0.9393	1.3677	1.7691	1.3677	0.9393	1.0000					6.3831
6	1.0000	0.9622	1.4104	1.8636	1.5531	1.6924	0.8019	1.1999				8.2836
7	1.0000	0.9763	1.4353	1.9115	1.6278	1.9115	1.4353	0.9763	1.0000			10.2739
8	1.0000	0.9857	1.4509	1.9392	1.6650	1.9979	1.6162	1.7410	0.8215	1.1999		12.2173
9	1.0000	0.9921	1.4615	1.9568	1.6864	2.0403	1.6864	1.9568	1.4615	0.9921	1.0000	14.2340

The required Ks and Q_{ex}s from the following equations [12,20]:

$$K_{i,i+1} = \frac{BW}{\sqrt{g_i \cdot g_{i+1}}}, \qquad \text{for } i=1 \text{ to } (N-1) \qquad (4)$$

$$Q_{ex1} = \frac{g_0 \cdot g_1}{BW} \qquad (5)$$

$$Q_{exN} = \frac{g_N \cdot g_{N+1}}{BW} \qquad (6)$$

where BW is the filter equal ripple fractional bandwidth given by

$$BW = \frac{\Delta f}{f_0} = \frac{f_{upper} - f_{lower}}{f_0} \qquad (7)$$

Once the required Ks and Q_{ex}s are known, Dishal's original method uses measured experimental hardware to generate two design curves. The first design curve is for coupling as a function of distance between two resonators that are tuned to the center frequency of the filter. The coupling curve might also relate some iris dimension to the coupling between resonators that are a fixed distance apart. To save space, narrowband filters often use tapped input and output resonators. The second design curve maps external Q to the position of the tap on the resonator. Once these design curves are available for a particular topology, it is a simple matter to map the desired Ks and Q_{ex}s to physical dimensions. Often some adjustment of dimensions is required in the filter prototype. Dishal's concepts can then be used to extract the realized Ks and Q_{ex}s from the prototype as a guide for tuning or modification. In short, the required two-resonator and single-resonator models have to be built in the EM field solver. With port tuning, it will also be obvious how to extract realized Ks and Q_{ex}s from the EM-based filter prototype. Only one design curve can be extracted from the Peano structure. This curve will correlate the coupling coefficients of the resonators with distance between them. The other curve, which correlates the feed tap positions with the external quality factor, cannot be extracted. This is attributed to the fact that the Peano resonator cannot provide a continuous physical contact with the feed taps along its whole length as in the case of quarter wavelength resonators used in parallel-coupled or hair-pin microstrip bandpass filters. Instead, manual tuning has to be carried out of the tap positions along the side lengths of the first and the last

ISSN 1813-2065

resonators of the resulting filter prototype and monitoring the filter responses until reaching the required performance.

For the proposed filter design, it has been postulated that the filter is with an N=4, centered at 2.45GHz, with a 10% fractional bandwidth. The lowpass prototype ripple level is 0.036dB (20.8dB return loss). No specific insertion loss or stopband rejection goals were set for this design. Table (1) and Eqs.(3)–(7), have been used to determine the corresponding values of $K_{1,2}$, $K_{2,3}$, $K_{3,4}$, and Q_{ex} as follows

$$K_{1,2} = \frac{BW}{\sqrt{g_1 g_2}} = \frac{0.1}{\sqrt{(0.8989)(1.2843)}} = 0.093,$$

$$K_{2,3} = \frac{BW}{\sqrt{g_2 g_3}} = \frac{0.1}{\sqrt{(1.2843)(1.5410)}} = 0.071,$$

$$K_{3,4} = \frac{BW}{\sqrt{g_3 g_4}} = \frac{0.1}{\sqrt{(1.5410)(0.7491)}} = 0.093,$$

and

$$Q_{ex4} \approx Q_{ex1} = \frac{g_0 g_1}{BW} = \frac{(1.0000)(0.8989)}{0.1} = 8.989$$

If we loosely couple to a pair of resonators tuned to the same frequency, we get the double peak response as shown in Fig. (2), [12,20]. The null between the two peaks should be at −30 dB to −40dB to guarantee loose coupling. The synchronous tuning condition occurs when the peaks are as close together as possible and/or when the null between the peaks is as deep as possible. The expression for the coupling coefficient is given by

$$K = \frac{f_{high} - f_{low}}{f_0} = \frac{f_{high}^2 - f_{low}^2}{f_{high}^2 + f_{low}^2} \qquad (8)$$

where f_{high} is the frequency of the upper peak and f_{low} is the frequency of the lower peak.

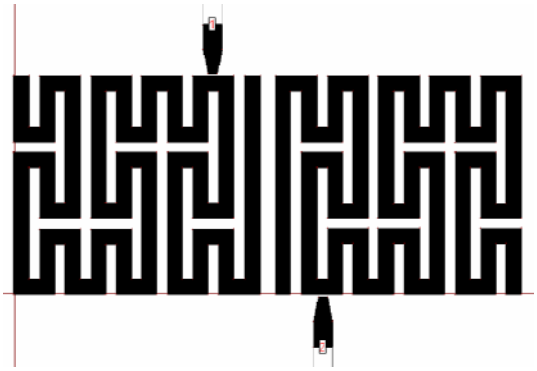

Fig. (2) A two loosely-coupled Peano resonators filter designed at a frequency of 2.45GHz to extract the coupling coefficient design curve

In Fig. (3), two resonators have been loosely coupled to input and output probes. To enhance a suitable capacitive coupling between the resonators, additional stub has been added to each resonator. This will lengthen the overall length of the resonator making it resonates at a lower frequency. It has been found that this stub provides a proper means to make the resonator resonates at the design frequency when modeling it in the EM simulator, [21]. In this case, the field solver will compute the same resonant frequency for both resonators. Based on Fig. (3), and Eq.(8), the value of the coupling coefficient is equal to 1.007, corresponding to a value of spacing between resonators of 0.3mm. The field solver data for four frequencies in the vicinity of the filter centre frequency has been needed. Therefore, three or four projects with different resonator spacing have to be run on the field solver and extract the coupling coefficient for each of them.

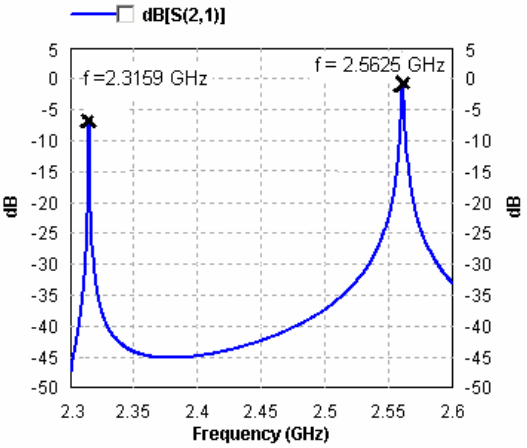

Fig. (3) The two-port transmission response for the two loosely parallel coupled synchronously tuned Peano resonators of Fig. (2). In this case, from Eq. (8), K=0.1007

If we then do a least-squares fit to a second-order polynomial function, the results in the design curve shown in Fig. (4). The fitted curve should pass through the data points with very low residual error. If the computed points cannot be fit to a low-order polynomial, the simulation method and the data extraction process should be repeated to check for errors [12]. Figure (5) shows the return loss and the insertion loss responses for the two Peano resonators filter (N=2). This response has clearly shown that the modeled filter has good characteristics at the lower cut-off passband, while it has less sharp characteristics at the higher cut-off. This is attributed to the slight dissymmetry of the surface current distribution on the conducting strips of this filter at the centre frequency, as shown in Fig. (6). In spite this slight dissymmetry in the filter response, the filter still has good in-band return loss of about -10.74dB and in-band ripple of about -0.45dB. The filter occupies an overall area of 3.7mm×8.92mm, which represents $(0.075\times0.086)\lambda_g$, with resonator dimensions of 3.7mm×4.17mm and spacing between the resonators of 0.58mm and a resonator strip width of 0.25mm.

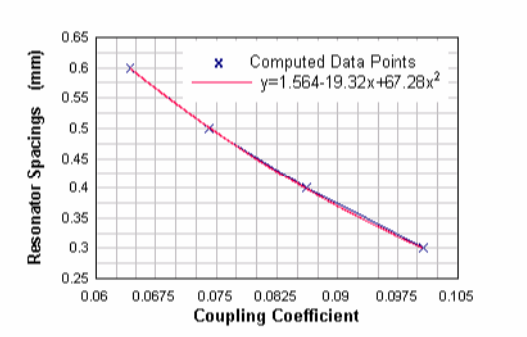

Fig. (4) The coupled Peano resonators spacing versus coupling coefficient for the geometry shown in Fig. (2)

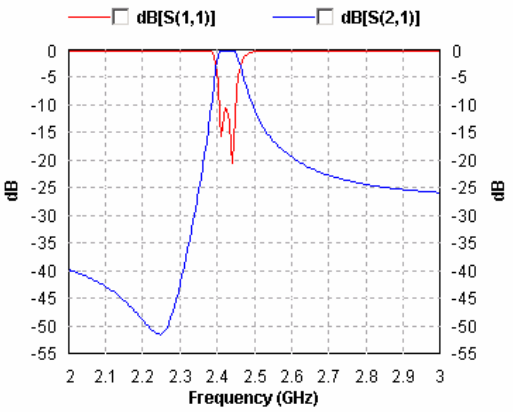

Fig. (5) The return loss S_{11} and the transmission S_{21} responses of the two coupled Peano resonator filter shown in Fig. (2)

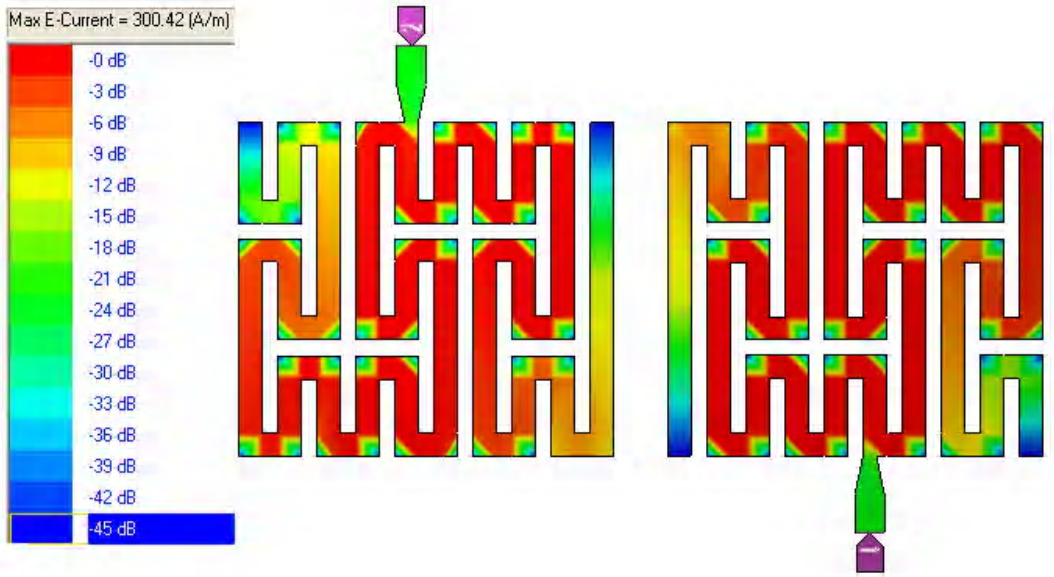

Fig. (6) The surface current distribution on the two coupled Peano resonator filter shown in Fig. (2) at 2.45GHz

4. Filter Performance Evaluation

The complete 4-pole Chebyshev bandpass filter model is now ready to be built in the EM field solver. A suitable grid, in the EM solver, has to be chosen to make a good compromise between geometrical resolution and solution time. In Fig. (4), $K_{1,2}$=$K_{3,4}$=0.093 implies a spacing of 0.3527mm, which we will round up to 0.35mm. $K_{2,3}$=0.071 implies a spacing of 0.5316mm, which was rounded up to 0.53mm.

The largest expected error is the tuning of the first and last resonators. It is well known for the filter designer that tapping has a major effect on resonator tuning. There is a need to perform some type of tuning to reach the required performance. The major tuning variables are the resonator spacing, and the tap position. Additional tuning for the inter-resonator spacing and the feeding tap positions has been carried out, in an attempt to reach design specifications.

Figure (7) shows the layout of the resulting modeled filter. The filter occupies an overall area of 3.7mm×17.42mm with previously stated Peano resonator dimensions. The spacing between the 1st and the 2nd resonators has become about 0.3mm, which is equal to the spacing between the 3rd and the 4th resonators, while the central spacing has become 0.55mm.

Figures (8-10) demonstrate the resulting performance curves after tuning. Filter responses shown in Fig. (8) imply symmetrical characteristics with sharper lower and higher cut-off passband, centered at a frequency of about 2.456GHz. The resulting fractional bandwidth is of about 2%, as indicated in the in-band response shown in Fig. (9). Increasing the bandwidth requires further tuning of the inter-resonators spacings. The price to be paid for this is the corresponding increase of the in-band ripple which worsens the overall filter performance. Redesigning the filter with greater

targeted bandwidth might be helpful to gain some increase in the resulting filter bandwidth as compared with that realized in the presented design. The in-band return loss and insertion loss are of about -0.19dB and -16.68dB, respectively, making the final filter prototype almost meets the predetermined design specifications. Figure (10) shows the out-of-band responses of this filter. The 2nd harmonic response appearing here is of little importance, since it is with a very narrow-band and low value of return loss, while the 3rd harmonic response has considerably diminished. To further improve the required response, filter order N has to be increased.

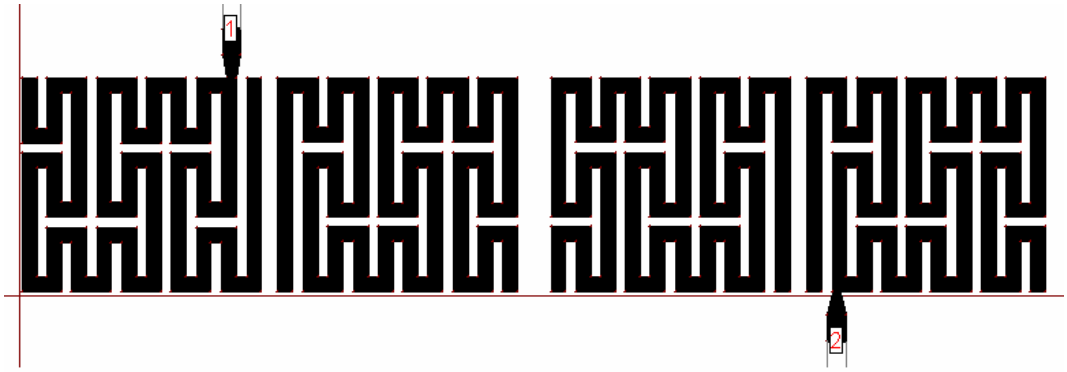

Fig. (7) The resulting layout of the 4-pole Chebyshev Peano resonator microstrip bandpass filter

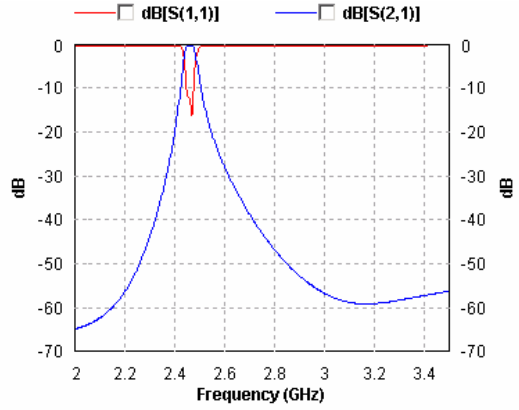

Fig. (8) The return loss S_{11} and the transmission S_{21} responses of the 4-pole Chebyshev Peano resonator bandpass filter shown in Fig. (7)

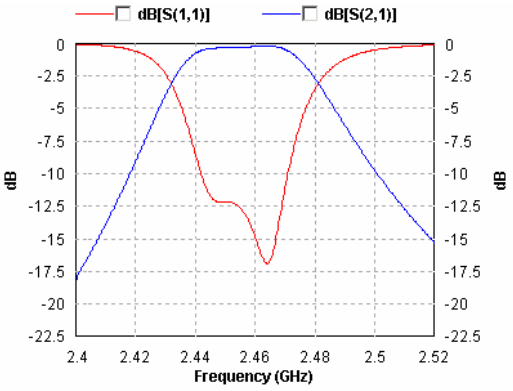

Fig. (9) The in-band return loss S_{11} and the transmission S_{21} responses of the 4-pole Chebyshev Peano resonator bandpass filter shown in Fig. (7)

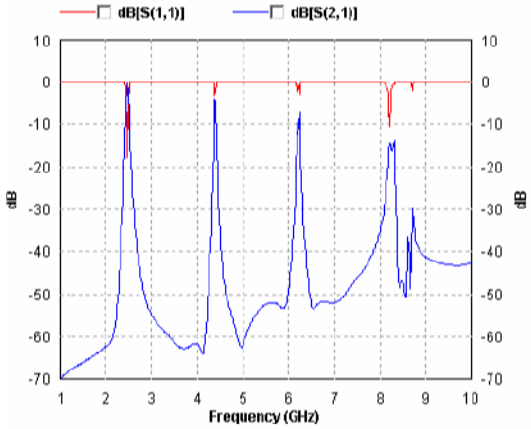

Fig. (10) The out-of-band return loss S_{11} and the transmission S_{21} responses of the 4-pole Chebyshev Peano resonator bandpass filter shown in Fig. (7)

5. Conclusions

A new multiresonator Chebyshev narrowband microstrip bandpass filter design for use in modern compact wireless communication systems has been presented in this paper. The proposed filter structure has been composed of coupled single-mode microstrip resonators in the form of 2nd iteration Peano fractal curve. The space-filling property of the proposed fractal structure, results in a high degree of miniaturization of the single mode resonators. Each resonator has been found to occupy an area of about $(0.075\times0.086)\lambda_g$. The resulting filter has reasonable passband performance besides the size reduction gained making it suitable for a wide variety of wireless communication applications. Furthermore, performance responses have shown that the proposed filter has less tendency to support higher harmonics which

conventionally accompany the bandpass filter performance.

Additional work has to be carried out to explore the promising features that might be offered by Chebyshev filters topologies based on the higher iteration Peano curve resonators. The possibility to design quasi-elliptic dual-mode microstrip ring resonator filters based on proposed fractal geometry has to be investigated.

References

[1] B.B. Mandelbrot, "**The fractal Geometry of Nature",** W. H. Freeman and Company (New York) (1983) 25.

[2] D.L. Jaggard, **"On Fractal Electrodynamics",** in H.N. Kritikos and D.L. Jaggard (eds.), Recent Advances in Electromagnetic Theory, Springer-Verlag, (1990) 183-224.

[3] O.I. Yordanov et al., "Prospects of Fractal Filters and Reflectors," *IEE 7th Inter. Conf. on Antenna and Propagation*, *ISCAP91,* York, UK, (1991) 698-700.

[4] J. Chen et al., *Prog. In Electromag. Res., PIER,* 70 (2007) 269-280.

[5] M. Barra et al., *Proc. IEEE Trans. on Appl. Superconductivity*, 15(3) (2005) 3841-3846.

[6] M.C. Barra et al., *Microwave Symp. Dig.*, *IEEE-MTT-S Int.*, (2004) 123-126.

[7] V. Crnojevic-Bengin, V. Radonic, and B. Jokanovic, "Complementary Split Ring Resonators Using Square Sierpinski Fractal Curves", *Proc. of the 36th European Microwave Conf.*, Manchester, UK, (2006) 1333-1335.

[8] G.L. Wu et al., *Prog. In Electromag. Res., PIER,* 78 (2008) 17-24.

[9] I.K. Kim et al., *J. Korean Electromag. Eng. Soc., JKEES*, 6(4) (2006) 1-10.

[10] J.K. Ali, "A New Miniaturized Fractal Bandpass Filter Based on Dual-Mode Microstrip Square Ring Resonator," *Proc. of the 5th Inter. Multi-Conf. on Signals, Systems and Devices, IEEE SSD'08,* Amman, Jordan, July 20-23, 2008.

[11] J.K. Ali, *Iraqi J. of Appl. Phys.*, *IJAP*, 5(1) (2009) 7-12.

[12] D.G. Swanson, *IEEE Microwave Mag.*, 5(8) (2007) 105-114.

[13] M. Dishal, *Proc. IRE*, 39 (1951) 1448–1455.

[14] H. Sagan, **"Space-Filling Curves",** Springer-Verlag (New York) (1994).

[15] J. Zhu, A. Hoorfar and N. Angheta, *IEEE Ant. Wireless Propag. Lett.*, 3 (2004) 71-74.

[16] J.P. Gianvittorio, "Fractals, MEMS, and FSS Electromagnetic Devices: Miniaturization and Multiple Resonances", Ph.D. thesis, University of California, U.S.A (2003) 8.

[17] K. Falconer, **"Fractal Geometry; Mathematical Foundations and Applications",** 2nd ed., John-Wiley & Sons, Ltd., (Chichester) (2003) 27.

[17] D.G. Swanson, Jr., and W.J.R. Hoefer, **"Microwave Circuit Modeling Using Electromagnetic Field Simulation",** Artech House (Dedham, MA) (2003) 378–384.

[18] H. Peitgen, H. Jürgens, D. Saupe, **"Chaos and Fractals",** New Frontiers of Science, 2nd Edition, Springer-Verlag (NY) (2004) 173.

[19] G.L. Matthaei, L. Young, and E.M.T. Jones, **"Microwave Filters, Impedance-Matching Networks and Coupling Structures",** McGraw-Hill, (NY) (1964) 85–95.

[20] J.S. Hong and M.J. Lancaster, **"Microstrip Filters for RF/Microwave Applications",** John-Wiley & Sons, Inc., (NY) (2001) 407.

[21] IE3D User's Manual, Release 14.1, Zeland Software Inc., Fremont, CA, May 2008.

ISSN 1813-2065

IRAQI JOURNAL OF APPLIED PHYSICS

Found in 2005, Find in 2009

By
Oday A. Hamadi
Managing Editor, IJAP

ENDING EVERY YEAR, the Editorial Board of IJAP works hard to diagnose and study its progress and interaction with the scientific research community in Iraq throughout collecting and analyzing the statistic data both quantitatively and qualitatively, as well as throughout the direct opinions extracted from samples based on time and field variety inside the scientific research community in Iraq. In this issue, the last of 2009 volume, we will preview the classification of the articles published in IJAP since its first issue in January 2005 ending with this current issue according to the nine branches of applied physics dedicated by IJAP. Also, we will preview the classification of authors of these articles as Iraqis, Arabs or Foreign. We think that both classifications may assist IJAP to proceed into the horizon of development and growth during the next years.

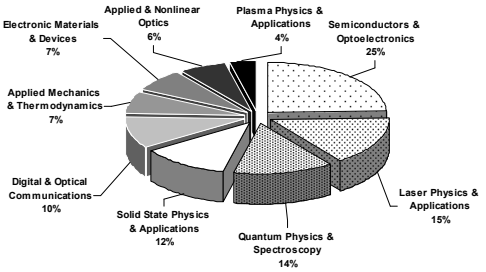

Articles published in IJAP (2005-2009) by subject

This study explains that about 25% of the published article were on *semiconductors & optoelectronics*, whereas 15% on *laser physics & applications*, 14% on *quantum physics & spectroscopy*, 12% on *solid state physics & applications*, 10% on *digital & optical communications*, 7% on *applied mechanics & thermodynamics*, 7% on *electronic materials & devices*, 6% on *applied & nonlinear optics* and 4% on *plasma physics & applications*. As well, this study explains that about 73% of authors were *Iraqis*, 25% *Foreign* and only 2% *Arabs*.

Accordingly, we can highlight some points from this analysis. The reality of scientific research in Iraq allowed Iraqi researchers – either individuals or groups – to work on *semiconductors & optoelectronics* much more than other fields. They work on solar cells, photodetectors, deposition and doping techniques (such as LID, PLD, CVD, PECVD, CBD, spray pyrolysis, etc.), crystal growth, production of nanostructures, optical and electrical properties of thin films, thermal annealing and photoconductivity. This may be attributed to the open technology, clearness of theories, availability of competed experts – either from foreign or national universities – and lower financial and technical requirements when compared to other fields.

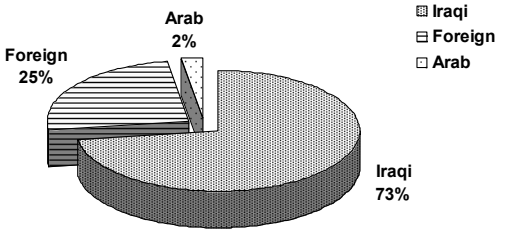

Authors of IJAP articles by nationality

The fields of high financial and technical requirements, such as *plasma physics & applications*, *applied & nonlinear optics*, *electronic materials & devices*, and *applied mechanics & thermodynamics*, have found less interest by Iraqi authors those published their articles in IJAP and most of the published articles in such fields were submitted by foreign authors. Most articles on *digital & optical communications*, *solid state physics & applications*, and *quantum physics & spectroscopy*, submitted by Iraqi authors, were dealing with simulation and modeling works, while the articles on *laser physics & applications* submitted by Iraqi authors have combined between experimental and theoretical works, however, such theoretical studies have based upon experimental results. This highlights the availability of good Iraqi experiences on laser physics and applications within the available possibilities and resources.

This study highlights that 50% of the published articles were on *semiconductors & optoelectronics*, *laser physics & applications*, and *digital & optical communications*, as the results and outcomes of these branches can applicably and directly be found over the academic and research fields as well as the daily life of the modern society.

Despite the acceptable echo of IJAP inside the scientific research community in Iraq and the interesting contributions from foreign authors, which represent a "record" over Iraqi and Arab scientific journals, the Arabic contributions still small. This is attributed mainly to the electronic distribution style considered by IJAP rather than the printed hard copies, which in turn due to the poor financial resources of IJAP. Otherwise, IJAP hard copies may be available in too many libraries in Arab universities. As well, the scientific research communities in Arab countries do not respond to Arabic scientific journals and periodicals as required that makes IJAP a new experiment among the Arab specialized scientific journals.

Haitham S. Dawood

School of Applied Sciences, University of Technology, Baghdad, Iraq

Analytical Equivalent Circuit of High-Irradiated Conventional Silicon Solar Cell Performance

In this study the current–voltage characteristics of a conventional silicon solar cell were studied. The experimental examination is carried out under a high concentration of light. The variations of the two reverse saturation currents are consistent with the physical significance of both the diffusion and the space-charge generation-recombination terms through their exponential variations. The simulation results clearly demonstrated that the solar cell is described with reasonable accuracy by a two-diode equivalent model that simulates the effects of the double-exponential dark current–voltage characteristics on the open-circuit voltage, fill factor, and conversion efficiency of the solar cell at a high concentration. The theoretical results are in good agreement with the experimental observations.

Keywords: Solar cells, Silicon-based devices, Equivalent circuit, High irradiation
Received: 20 July 2009, **Revised**: 22 September 2009, **Accepted**: 27 September 2009

1. Introduction

The presence of a p-n junction in a semiconductor makes solar power possible. The space charge region is formed as a result of the diffusion of majority carriers across the metallurgical junction, and its width is fixed when the diffusion is counter balanced by the drift of carriers in the opposite direction, thus setting up a compact but strong electric field as the collecting junction in the depletion region [1]. In thermal equilibrium, drift and diffusion currents through the depletion region oppose each other, resulting in zero net current flow. Using light as an external stimulus allows the p-n junction to behave as follows. Part of the solar spectrum is absorbed in a semiconductor through the transfer of optical energy to electrons that are excited into the conduction band creating holes in the valence band. The electric field in the depletion region helps in separating these electron-hole pairs, resulting in a voltage or the photovoltaic effect [2].

The efficiency of photovoltaic solar cells decreases with an increase in temperature [3]. When silicon solar cells are used under concentrated sunlight they tend to heat up [4], as a result of which the current and voltage generated by the solar cell are modified. An excessive rise in the solar cell temperature has degrades effects on the solar cell characteristics. In general, the open-circuit voltage (V_{OC}) decreases rapidly and the short circuit current (I_{SC}) increases slowly, as the temperature rises.

In this paper, we present a modeling analysis implemented to introduce the I–V characteristics of silicon-based solar cells at high light concentration. The correlations between experimental I–V plots and theoretical counterparts under different illumination intensities are studied.

The model must take into account the various recombination and generation processes in the solar cell under illumination. Thus, the device can be modeled with either the conventional single-diode model or the two-diode model.

Under illumination, the cell may be represented by an equivalent circuit based on a single-diode model, as shown in Fig. (1). The cell is described as a current source in parallel with the junction as

$$I = I_{ph} - \frac{V + IR_S}{R_{sh}} - I_0\left\{\exp\left[\frac{q}{nKT}(V + IR_S)\right] - 1\right\} \qquad (1)$$

where I_{ph} represents the photocurrent, I_0 is the saturation current under reverse bias; R_S and R_{sh} are respectively series resistance and shunt resistance, n is the ideality factor, q is the elementary electron charge, k is the Boltzmann constant and T is the temperature.

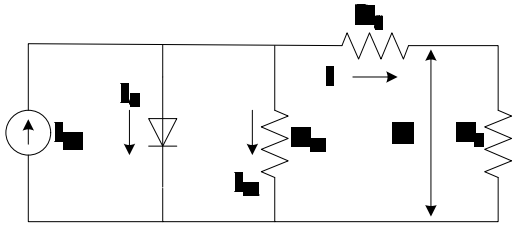

Fig. (1) Single-diode model of a solar cell under high irradiation condition

The simplified two-diode model of a solar cell may be described by the new lumped parameter simplified equivalent circuit shown in Fig. (2) [5,6]. For a given incident light intensity, at a given temperature, the implicit I–V relationship is given by

$$I = I_{ph} - \frac{V + IR_S}{R_{sh}} - I_{01}\{\exp[B_1(V + IR_S)] - 1\} - I_{02}\{\exp[B_2(V + IR_S)] - 1\} \quad (2)$$

where $B_1=q/kT$, $B_2=B_1/n$ and I_{01} represents the saturation current originating from the quasi neutral region of the junction which is affected by, as diffusion, recombination and the drift effect [5]; I_{02} corresponds to the carrier recombination via deep levels in the space-charge region of the junction [6]. The reverse saturation current I_{02} is generally 3 to 7 orders of magnitude larger than I_{01}; the diode quality factor n=2 for the approximation corresponding to the Shockley–Read–Hall recombination current in the space-charge region [5,7]; n is also a fitting parameter that is greater than 2.

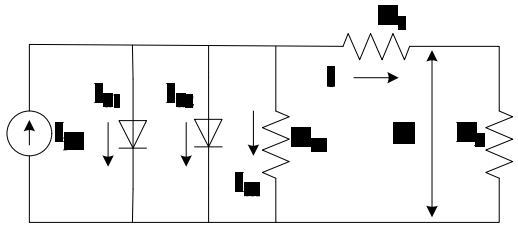

Fig. (2) Double-diode model of a solar cell under high irradiation condition

The experimental study of the temperature dependence of I_{01} and I_{02} should help to verify their different origins. Such studies have been previously published under dark conditions [8]. It is interesting to determine the temperature dependencies of electrical parameters while the cell is operating as a generator under illumination. It should be noted that the illumination does not cause a simple translation of the I–V characteristics along the current axis [9,10], the series resistance effect is non-linear and the injection level changes from low to high level. Several methods have been proposed for the determination of the free parameters in this model from the I–V measurements [11,12].

In order to present general approach for calculating all the cell parameters, we use Eq. (2), for the two following special cases.

(i) For $V=V_{OC}$ and I=0

$$0 = I_{ph} - \frac{V_{OC}}{R_{sh}} - I_{01}\{\exp[B_1(V_{OC} + IR_S)] - 1\} - I_{02}\{\exp[B_2(V_{OC} + IR_S)] - 1\} \quad (3)$$

(ii) For $I=I_{SC}$ and V=0

$$I_{SC} = I_{ph} - \frac{I_{sh}R_S}{R_{sh}} - I_{01}\{\exp[B_1(I_{SC}R_S)] - 1\} - I_{02}\{\exp[B_2(I_{SC}R_S)] - 1\} \quad (4)$$

Differentiating Eq. (2) with respect to I on both sides for the two special cases considered above we have

(i) For I=0, $V=V_{OC}$, one can write

$$1 = \left(\left.\frac{dV}{dI}\right|_{V=V_{OC}} + R_S\right)\left(-\frac{1}{R_{sh}} - I_{01}B_1\exp[B_1(V_{OC})] - I_{02}B_2\exp[B_2(V_{OC})]\right) \quad (5a)$$

where

$$R_{S0} = -\left.\left(\frac{dV}{dI}\right)\right|_{V=V_{OC}}$$

Thus, R_S is given as

$$1 = -\left(\left.\frac{dV}{dI}\right|_{V=V_{OC}} + R_S\right)\left(\frac{1}{R_{sh}} + I_{01}B_1\exp[B_1(V_{OC})] + I_{02}B_2\exp[B_2(V_{OC})]\right) \quad (5b)$$

Re-arranging

$$-\left.\frac{dV}{dI}\right|_{V=V_{OC}} - R_S = \frac{1}{\left(\frac{1}{R_{sh}} + I_{01}B_1\exp[B_1(V_{OC})] + I_{02}B_2\exp[B_2(V_{OC})]\right)} \quad (5c)$$

$$R_S = R_{S0} - \frac{1}{\frac{1}{R_{sh}} + I_{01}B_1\exp[B_1(V_{OC})] + I_{02}B_2\exp[B_2(V_{OC})]} \quad (6)$$

(ii) For V=0, $I=I_{SC}$, we obtain

$$1 = \left(\left.\frac{dV}{dI}\right|_{I=I_{SC}} + R_S\right)\left(-\frac{1}{R_{sh}} - I_{01}B_1\exp[B_1(I_{SC}R_S)] - I_{02}B_2\exp[B_2(I_{SC}R_S)]\right) \quad (7)$$

where

$$R_{sh0} = -\left.\left(\frac{dV}{dI}\right)\right|_{I=I_{SC}}$$

Thus

$$R_S = \frac{1}{\frac{1}{R_{sh0} - R_S} - I_{01}B_1 \exp\left[B_1(I_{SC}R_S)\right] - I_{02}B_2 \exp\left[B_2(I_{SC}R_S)\right]} \quad (8)$$

For $V=V_{OC}$ and $I=I_{SC}$, we have

$$I_{ph} = \frac{V_{OC}}{R_{sh}} + I_{01}\left\{\exp\left[B_1 V_{OC}\right] - 1\right\} - I_{02}\left\{\exp\left[B_2 V_{OC}\right] - 1\right\} \quad (9)$$

Equations (3), (4), (6), (8), and (9) form a system of simultaneous equations where the unknown parameters are R_S, R_{sh}, I_{01}, I_{02}, and I_{ph} respectively. To be very general, let

$u=R_S$, $v=R_{sh}$, $x=I_{ph}$, $y=I_{01}$, $z=I_{02}$ (10)

The system can be written as

$$\begin{aligned} f_1(u,v,x,y,z) &= 0 \\ f_2(u,v,x,y,z) &= 0 \\ f_3(u,v,x,y,z) &= 0 \\ f_4(u,v,x,y,z) &= 0 \\ f_5(u,v,x,y,z) &= 0 \end{aligned} \quad (11)$$

The system in Eq. (11) is resolved numerically using the Newton–Raphson algorithm of the form

$$\begin{bmatrix} v_k \\ w_k \\ x_k \\ y_k \\ z_k \end{bmatrix} = \begin{bmatrix} v_{k-1} \\ w_{k-1} \\ x_{k-1} \\ y_{k-1} \\ z_{k-1} \end{bmatrix} - \begin{bmatrix} \frac{\partial f_1}{\partial u} & \frac{\partial f_1}{\partial v} & \frac{\partial f_1}{\partial x} & \frac{\partial f_1}{\partial y} & \frac{\partial f_1}{\partial z} \\ \frac{\partial f_2}{\partial u} & \frac{\partial f_2}{\partial v} & \frac{\partial f_2}{\partial x} & \frac{\partial f_2}{\partial y} & \frac{\partial f_2}{\partial z} \\ \frac{\partial f_3}{\partial u} & \frac{\partial f_3}{\partial v} & \frac{\partial f_3}{\partial x} & \frac{\partial f_3}{\partial y} & \frac{\partial f_3}{\partial z} \\ \frac{\partial f_4}{\partial u} & \frac{\partial f_4}{\partial v} & \frac{\partial f_4}{\partial x} & \frac{\partial f_4}{\partial y} & \frac{\partial f_4}{\partial z} \\ \frac{\partial f_5}{\partial u} & \frac{\partial f_5}{\partial v} & \frac{\partial f_5}{\partial x} & \frac{\partial f_5}{\partial y} & \frac{\partial f_5}{\partial z} \end{bmatrix}^{-1}_{(u_{k-1},v_{k-1},x_{k-1},y_{k-1},z_{k-1})} \cdot \begin{bmatrix} f_1(u_{k-1},v_{k-1},x_{k-1},y_{k-1},z_{k-1}) \\ f_2(u_{k-1},v_{k-1},x_{k-1},y_{k-1},z_{k-1}) \\ f_3(u_{k-1},v_{k-1},x_{k-1},y_{k-1},z_{k-1}) \\ f_4(u_{k-1},v_{k-1},x_{k-1},y_{k-1},z_{k-1}) \\ f_5(u_{k-1},v_{k-1},x_{k-1},y_{k-1},z_{k-1}) \end{bmatrix} \quad (12)$$

---

where the initial conditions are thus given by

$$\begin{bmatrix} u(1) \\ v(1) \\ x(1) \\ y(1) \\ z(1) \end{bmatrix} = \begin{bmatrix} 0 \\ 0 \\ 0 \\ 0 \\ 0 \end{bmatrix} \quad (13)$$

The five different parameters of the single-diode model, can be determined directly from the latter equations using $I_{01}=0$ and $I_{02}=I_0$.

2. Experiment

In this work, we have used standard solar panel fabricated by Hebe Solar Co., Ltd. (China) in order to test the model at optimum solar parameters. The panel is 15x15cm in area and partitioned into many multicrystalline silicon p-n junction solar cells. Each cell is 25x25mm in dimensions, 300μm in thickness and delivers 40% more power than customary cells. The front grid was made of 2 silver bus bars, 1mm wide, with about 80 fingers of 5μm length between them and SiN_x AR coating. The back side contains of 5mm wide soldering pads (Ag/Al) and back surface field (Al). The contact thickness was 2.5μm and the sheet resistance was 900Ω/□. The cells were mounted on thermal-clad substrates, which are commonly used for hybrid electronic circuits. The n-type side was 200nm thick with a doping density of $2x10^{18}cm^{-3}$ and the p-type side was 800nm thick with a doping density of $2x10^{17}cm^{-3}$. The maximum efficiency of this cell as illustrated by the manufacturer is ranging within 13.8-15.6% at 3.5W maximum output power. The conversion measurements were conducted under solar radiation. The concentrator system used is advantageous for giving good illumination uniformity at the focus. The focus was $3X3cm^2$ in area and was slightly larger than the dimensions of the tested cells.

The measured parasitic resistance induced by this set-up was in the order of 20mΩ which is a minimal contribution for the tested cells. Under the same experimental conditions, a solar cell

ISSN 1813-2065

operating at a high concentration of light shows only slight degradation as a result of the parasitic effect.

3. Results and Discussion

The equivalent-circuit parameter values were determined and the simulated I–V plots together with the experimental counterparts are represented in Figs. (3–6) for four different concentrations. The simulated parameters were calculated using the single-diode model and the two-diode model presented above. A Comparison between the cell parameters obtained using each model with the corresponding experimental values was conducted to find the best model.

The results clearly show that the proposed two-diode model is compatible with the solar cell at high concentrations (X=73:36, 139.27, and 201.19). On the other hand, the single-diode model seems better for the low concentration of X=1 where the two-diode model is less precise than the single-diode model.

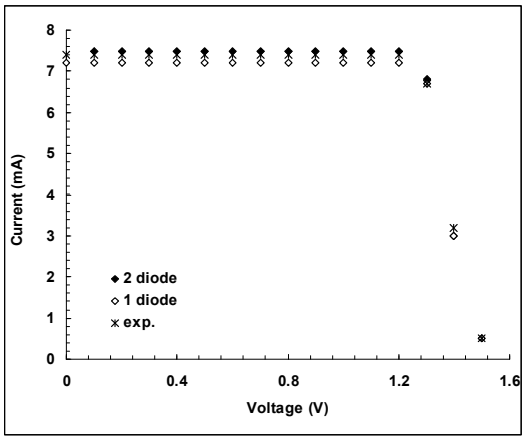

Fig. (3) Simulated curves and experimental measurements of I–V characteristics of the solar cell under concentration level of X=1 (X is the light concentration level)

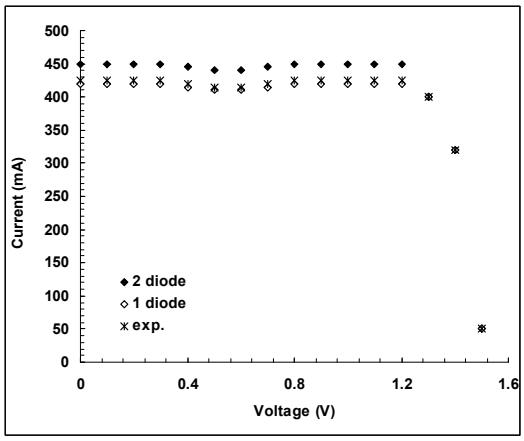

Fig. (4) Simulated curves and experimental measurements of I–V characteristics of the solar cell under concentration level of X=73:36 (X is the light concentration level)

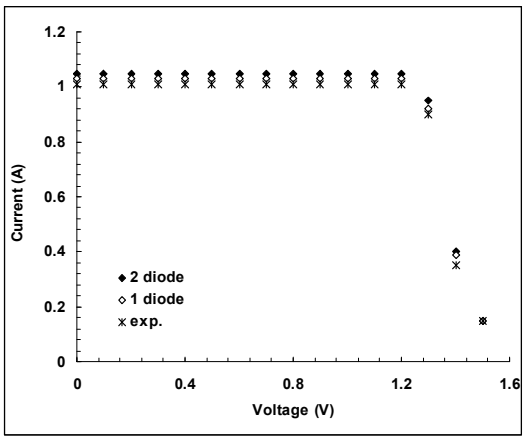

Fig. (5) Simulated curves and experimental measurements of I–V characteristics of the solar cell under concentration level of X=139:27 (X is the light concentration level)

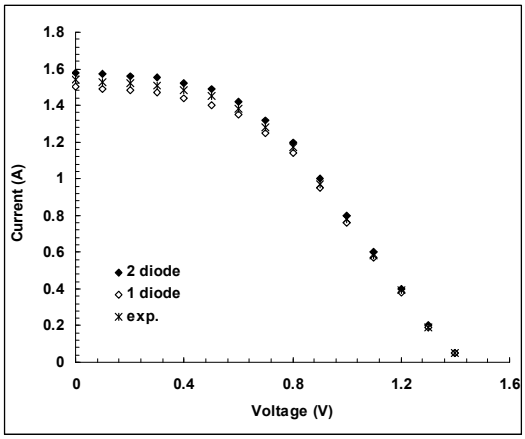

Fig. (6) Simulated curves and experimental measurements of I–V characteristics of the solar cell under concentration level of X=201:19 (X is the light concentration level)

At high levels of solar concentration, the good agreement of experimental results with the two-diode model can be explained by the fact that under such conditions the traps, which are susceptible to intervening in the recombination, are saturated and the amount of diffusion becomes significant. The two-diode model can be applied under conditions of weak injection, while taking in account three essential mechanisms [7]. First, the diffusion takes into account the recombination mechanisms in the quasi-neutral regions (notably the contacts). Second, the recombination in the space-charge region of the junction, by the recombinant centers associated with the levels situated in the strip forbidden for a homojunction represented by one exponential term. Finally, Joule effect is translated into losses due to the series resistance and shunt resistance.

Therefore the two-diode model is the more suitable for the precise simulation of a solar cell in a real situation [1,5,10]. This is presumably due to the minority carrier diffusion process,

which becomes dominant in the conduction mechanisms at a high concentration of light [1,2].

4. Conclusions

The effects of double-exponential dark current–voltage characteristics on the different parameters of a silicon-based solar cell operating at high concentration of light were studied. The two-diode model was compared to the single-diode one in terms of the agreement between the simulated cell parameters and experimental values. We conclude that the conventional single-diode model is inadequate for describing the behavior of the studied device under high light concentration and that the two-diode model is more appropriate.

Acknowledgment

Author would like to thank Dr. R.M. Ibrahim for his valuable comments and notes. He also would like to thank Prof. M.A. Habeeb for his assistance in numerical analysis. Finally, he thanks Mr. S.I. Al-Hadithi at Thin Films Laboratory, University of Baghdad for experimental assistance and measurements.

References

[1] M. Masaki and M. Tatsuo, *Jpn. J. Appl. Phys. Part* 1, 45(1B) (2006) 542-545.

[2] T.K.P. Wong, *Electron. Lett.*, 32(3) (1996) 252 – 253.

[3] D. Meneses-Rodrıguez, P.P. Horley, J. Gonzalez-Hernandez, Y.V. Vorobiev and P.N. Gorley, *Solar Energy*, 78 (2005) 243.

[4] R.V. Singh and C.M. Singal, *Solar Cells,* 10 (1983) 155.

[5] T.K.P. Wong and P.C.H. Chan, An equivalent circuit approach to solar cell modeling, *IEEE Region 10 Inter. Conf. on Microelectronics and VLSI*, 1995, TENCON 95, 6-10 (November 1995) 222-225.

[6] G.L. Araujo, E. Sanchez and M. Marti, *Solar Cells*, 5 (1982) 199.

[7] J.-P. Charles, A. Haddi, A. Maouad, H. Bakhtiar, A. Zerga, A. Hoffmann and P. Mialhe, *Rev. Energy Ren.,* 3 (2000) 1.

[8] F. Lindholm, J. Fossum and E. Burgess, *IEEE Trans. Electron. Devices*, 26 (1979) 165.

[9] R.N. Hall, *Solid State Electron.*, 24 (1981) 595.

[10] J.-P. Charles, I. Mekkaoui-Alaoui and G. Bordure, *Solid State Electron.*, 28 (1985) 807.

[11] R.A. Kumar, M.S. Suresh and J. Nagaraju, *IEEE Trans. on Electron. Devices*, 48(9) (2001) 2177-2179.

[12] A. Cheknane, H.S. Hilal, F. Djeffal, B. Benyoucef and J.-P. Charles, *Microelectron. J.*, 39(10) (2008) 1173-1180.

 ISSN 1813-2065

2009 Physics Nobel Prize
Kao, Boyle & Smith

The Iraqi Journal of Applied Physics is proud to present a brief on this year's Nobel Laureates in Physics, Drs. Willard Boyle and George Smith, formerly of Bell Labs, for their invention of the charge-coupled device; and Dr. Charles Kao, of Standard Telecommunication Laboratories, Harlow, UK, and Chinese University of Hong Kong, for his work in development of optical fibers for telecommunications.

The part of this year's award associated with Mr. Kao underscores the fact that optical fibers carry an increasing fraction of phone calls, television programs, and internet traffic into homes. Data can move down silicon fiber more quickly than through copper wire because nothing is faster than light, and light signaling offers higher bandwidth for electronic circuitry. Encoding information in the form of light pulses rather than as electric pulses allows more data to flow down a line. Kao's principal achievement was in making the fiber more efficient; by excluding impurities in the fiber material, he developed a material that absorbed less of the light carrying signals over long distances.

The part of the prize associated with Boyle and Smith recognizes the huge advantage of capturing images in digital rather than film form. Pictures can be sent through wires more easily, can be manipulated and processed in creative ways (e.g., you can see a moving comet or supernova in sky scans by subtracting tonight's pixel map from last night's map), and can be stored more handily. Devices such as photomultiplier tubes for converting light into an electric signal have been around for decades. But the CCD allowed whole two-dimensional fields of optical data to be read out more quickly and efficiently. And, of course, CCD's have been the backbone of the commercial digital camera industry.


Charles Kao


Willard Boyle


George Smith

Overview of optical fibers and charge-coupled devices

THE 2009 NOBEL PRIZE IN PHYSICS will be awarded to **Charles K. Kao** (Standard Telecommunication Laboratories, Harlow, UK, and Chinese University of Hong Kong), and **Willard S. Boyle** and **George E. Smith** (both of whom worked chiefly at Bell Laboratories, in Murray Hill, NJ, USA) for their work leading to modern telecommunications. Kao will receive half the prize money for helping to invent modern optical fiber, allowing signals to travel flawlessly thousands of miles. Boyle and Smith will split the other half of the prize for their development of charge coupled devices (CCDs).

"The [transfer of] information in society today is completely based on [this research]," said Joseph Nordgren, the chair of the Nobel Prize committee in a press conference announcing the prize. "The practical implications for this research were enormous...It is something that has changed our life, not just in science but in society as whole."

Fred Dylla, CEO of the American Institute of Physics, which publishes *Physics Today*, concurs. "When combined with the laser and the transistor, the invention of an efficient, low-loss optical fiber has made nearly instantaneous communication possible across the entire globe. This mode of communication is essential for high-speed internet and forms the optical backbone of 21st century commerce. The CCD sensor has revolutionized technical, professional, and consumer photography in the last few decades. Taken together these inventions may have had a greater impact on humanity than any others in the last half century."

"Optics technologies are exceptionally significant for scientific developments in today's world," said Elizabeth Rogan, CEO, of the Optical Society of America. "We congratulate Kao, Boyle and Smith on this much-deserved recognition."

Kao

In 1966, Charles K. Kao made a discovery that led to a breakthrough in fiber optics. He carefully calculated how to transmit light over long distances via optical glass fibers. With a fiber of purest glass it would be possible to transmit light signals over 100 kilometers, compared to only 20 meters for the fibers available in the 1960s. "It was the impurities, and other limiting factors such as scattering, atomic motion, that limited glass fibers in the 1960s," said Nordgren.

Kao presented his research at the 1966 London meeting of the Institution of Electrical Engineers. The first ultrapure fiber was successfully fabricated just four years later, in 1970 by the Corning company.

"The Nobel Prize isn't awarded for lifetime achievement, it is given for diverse research, clearly Kao's work achieved a breakthrough that led to a whole new research and technology field," said Nordgren.

Boyle and Smith

In 1969 Willard S. Boyle and George E. Smith invented the first successful imaging technology using a digital sensor, a CCD (charge-coupled device).

The two researchers came up with the idea in just an hour of brainstorming, according to Boyle who spoke during a press conference today. "It is amazing that a [the CCD device] was created so quickly," said Nordgren. "There are so many breakthroughs that came out of research at Bell labs...it's unfortunate that during the 80s, US companies abandoned the idea of having a scientific environment such as Bell labs," said Nordgren.

Boyle said that to him, the biggest achievement of his work was seeing images transmitted back from Mars. "It wouldn't have been possible without our invention," he said.

The CCD technology makes use of the photoelectric effect, as theorized by Albert Einstein and for which he was awarded the 1921 Nobel Prize. By this effect, light is transformed into electric signals. The challenge, when designing an image sensor, was to gather and read out the signals in a large number of image points, pixels, in a short time.

The CCD is the digital camera's electronic eye. It revolutionized how images were collected from spacecraft, by telescopes, and in medical imaging, and has eventually replaced the film camera in every aspect of photography.

Edited by
Oday A. Hamadi
Managing Editor, IJAP

Comparison of the Radiation Characteristics of Triangular and Quadratic Koch Fractal Dipole Wire Antennas

Fawwaz J. Jibrael
Zahraa F. Mizeel

Department of Electrical and Electronic Engineering, University of Technology, Baghdad, Iraq

In this paper, a small size, low profile and multiband triangular and quadratic Koch curve dipole antenna are presented. The proposed antennas design, analysis and characterization had been performed using the method of moments (MoM). The designed antennas have operating frequencies of 603MHz, and 1789MHz for triangular Koch dipole antenna and 460MHz and 1262MHz for quadratic Koch dipole antenna. The radiation characteristics, reflection coefficients, VSWR, gain, and input impedance of the proposed antennas are described and simulated using the 4NEC2 software package.

Keywords: Fractal dipole antenna, Koch curve, Multiband antenna, Compact size antenna
Received: 20 July 2009, **Revised**: 22 September 2009, **Accepted**: 27 September 2009

1. Introduction

In modern wireless communication systems and in other increasing wireless applications, wider bandwidth, multiband and low profile antennas are in great demand for both commercial and military applications. This has initiated antenna research in various directions. One of which is using fractal shaped antenna element. Fractal geometries have three common properties, self-similarity, space-filling and fractal dimension. It has been shown that, the self-similarity property of fractal shapes can be successfully applied to the design of multiband fractal antennas and the space-filling property of fractals can be utilized to reduce antenna size. Fractal curves are well known for their unique space-filling properties [1], while the fractal dimension property has been widely used to discriminate fractal geometries from Euclidean.

Fractals were first defined by Mandelbrot in [2] as a way of classifying structures whose dimensions where not whole numbers. These geometries have been used previously to characterize unique occurrence in nature where difficult to define with Euclidean geometries, including the length of coastline, density of clouds, and the branching of trees [3].

The term “fractal” derived from the Latin word fractus, which means broken or irregular fragments [4]. Therefore, there is need for a geometry that handles these complex shapes better than Euclidean geometry, where the Euclidean geometry has a whole number of dimensions, such as a one dimensional line, or two dimensional planes...etc [3].

In antennas design, the use of fractal shapes makes the operational frequency of an antenna which depends on the ratio of the electromagnetic signal's wavelength to the physical size of the antenna independent of its scale. This means that a fractal antenna can be constructed in small sizes, yet possessing a broad frequency range [5]. The reason why the fractal design of antennas appears as an attractive way to make antennas is two reasons; firstly because one should expect a self-similar antenna (which contains many copies of itself at several scales) to operate in a similar way at several wavelengths. That is, the antenna should keep similar radiation parameters through several bands. Secondly, because the space-filling properties of some fractal shapes (the fractal dimension) might allow fractally-shaped small antennas to better take advantage of the small surrounding space [6].

2. Generation of Triangular Koch Curve

The method of construction of the Koch curve is illustrated in Fig. (1). The Koch curve is simply constructed using an iterative procedure beginning with the initiator of the set as the unit line segment (step n=0 in the figure). The unit line segment is divided into thirds, and the middle third is removed. The middle third is then replaced with two equal segments, both one-third in length, which form an equilateral triangle (step n=1); this step is the generator of the curve. At the next step (n=2), the middle third is removed from each of the four segments and each is replaced with two equal segments as before. This process is repeated to infinite number of times to produce the Koch curve. A noticeable property of the Koch curve is that it is seemingly infinite in length. This may be seen from the construction process. At each step n, in its generation, the length of the pre-fractal curve increases to $4/3L_{n-1}$, where L_{n-1} is the length of the curve in the preceding step [2].

ISSN 1813-2065

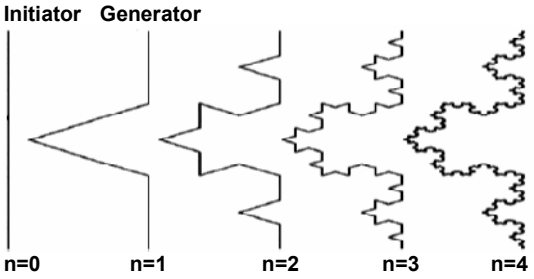

Fig. (1) The first four iterations in the construction of the triangular Koch curve

Fractal dimension contains used information about the self-similarity and the space-filling properties of any fractal structures [2]. The fractal similarity dimension (*FD*) is defined as [7]:

$$FD = \frac{\log(N)}{\log(1/\varepsilon)} = \frac{\log(4)}{\log(3)} = 1.26186$$

where N is the total number of distinct copies, and $(1/\varepsilon)$ is the reduction factor value which means how will be the length of the new side with respect to the original side length.

3. Generation of Quadratic Koch Curve

Figure (2) Contains the first three iterations in the construction of the quadratic Koch curve. This curve is generated by repeatedly replacing each line segment, composed of four quarters, with the generator consisting of eight pieces, each one quarter long (see Fig. 2) [7]. Each smaller segment of the curve is an exact replica of the whole curve. There are eight such segments making up the curve, each one represents a one-quarter reduction of the original curve.

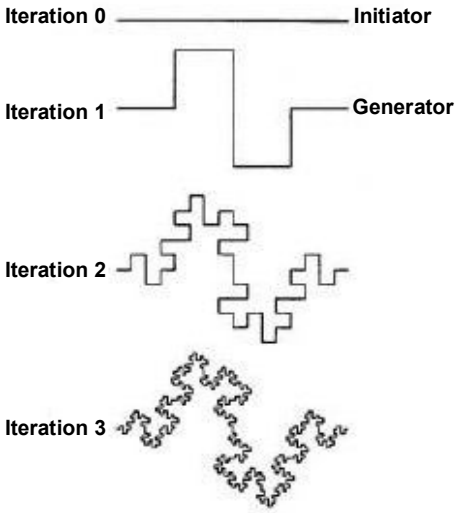

Fig. (2) First three iterations of the construction of the quadratic Koch curve

Different from Euclidean geometries, fractal geometries are characterized by their non-integer dimensions. Fractal dimension contains used information about the self-similarity and the space-filling properties of any fractal structures [2]. The fractal similarity dimension (*FD*) is defined as [7]:

$$FD = \frac{\log(N)}{\log(1/\varepsilon)} = \frac{\log(8)}{\log(4)} = 1.5$$

where N is the total number of distinct copies, and $(1/\varepsilon)$ is the reduction factor value which means how will be the length of the new side with respect to the original side length.

4. Design of the Triangular and Quadratic Koch Dipole Antennas

The triangular and quadratic Koch antennas which positioned in the YZ-plane has been simulated using numerical modeling commercial software 4NEC2, which is method of moment based software. The 4NEC2 program is used in all simulations. This is very effective in analyzing antennas that can be modeled with wire segments. The feed source point of these antennas are placed at origin (0,0,0), and this source set at 1V. The design frequency has been chosen to be 750MHz for which the design wavelength λ is 0.4m (40cm) then the length of the corresponding λ/2 dipole antenna length will be of 20cm. Figure (3) shows the visualization of triangular and quadratic dipole antenna geometry by using NEC-viewer software.

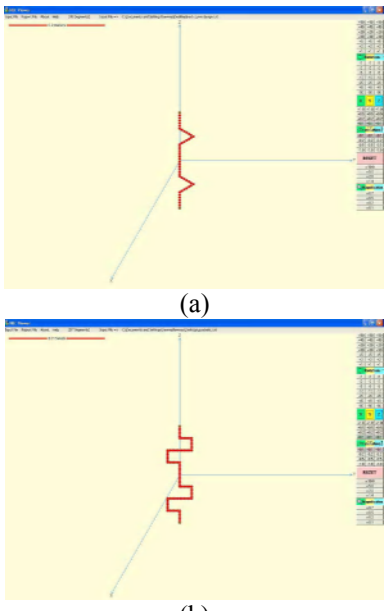

(a)

(b)

Fig. (3) Visualization of the modeled dipole antennas geometry of (a) triangular Koch antenna (b) Quadratic Koch antenna

5. Simulation Results of the Triangular Koch Dipole Antenna

The input impedance and radiation characteristics of this type of antenna have been widely studied by numerical simulations. From method of moment, the program will be able to

compute real and imaginary parts of the input impedance over the frequency range from 0 GHz to 3GHz, the resulting input impedance (both real and imaginary parts) are shown in Fig. (4), where the input impedance of the antennas with generalized Koch curves for the 1st iteration and 60° indentation angle are plotted, and this figure shows that the antenna has two resonance frequencies (603MHz and 1789MHz). At these frequencies, the imaginary parts of the input impedance is approximately zero.

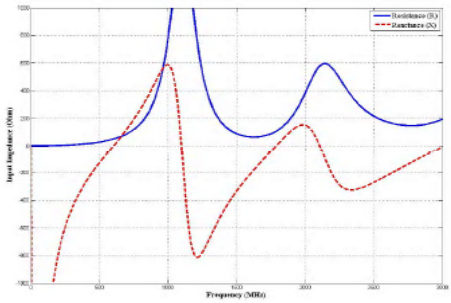

Fig. (4) Input Impedance for the 1st iteration Triangular Koch Curve

Table (1) shows the resonance frequencies and the corresponding input impedance, voltage-to-standing wave ratio (VSWR), and reflection coefficient values for each resonance frequency and table (2) shows the gain at each frequency in the XZ-plane and YZ-plane for the triangular Koch dipole antenna.

Table (1) Resonant frequencies and their input impedance, reflection coefficient and VSWR

Frequency (MHz)	Input Impedance (Ω)		VSWR	Reflection coefficient (dB)
	R	X		
603	50.7877	-j0.0376	1.01577	-42.131
1789	107.328	-j0.442	2.14661	-8.7686

Table (2) The gain of the proposed antenna at the resonant frequencies in the two planes

F(MHz)	Gain (dBi)	
	XZ-plane (phi=0°)	YZ-plane (phi=90°)
603	2.08	2.04
1789	2.97	3.22

The antenna reflection coefficient with respect to 50Ω transmission lines was plotted in Fig. (5) and the voltage-to-standing wave ratio (VSWR) is plotted in Fig. (6). The normalized electric field patterns in the three planes (XY-plane, XZ-plane, and YZ-plane) are plotted in Fig. (7) for each resonant frequency.

6. Simulation Results of the Quadratic Koch Dipole Antenna

The input impedance is shown in Fig. (8), which shows that the antenna has two resonance frequencies (460MHz and 1262MHz). At these frequencies, the imaginary parts of the input impedance approximately zero. Table (3) shows the resonance frequencies and the corresponding input impedance, VSWR, and reflection coefficient values for each resonance frequency and table (4) shows the gain at each frequency in the XZ-plane and YZ-plane for the quadratic Koch dipole antenna.

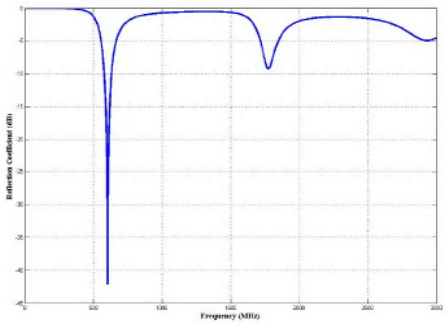

Fig. (5) Reflection coefficient at the antenna terminals

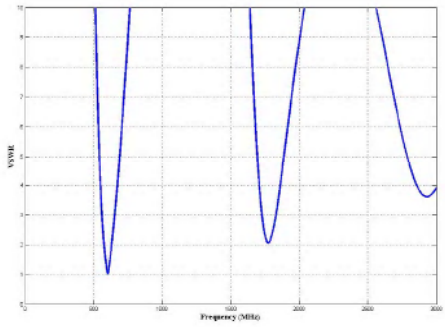

Fig. (6) Voltage to standing wave ratio (VSWR) at the antenna terminals

Table (3) Resonant frequencies and their input impedance, reflection coefficient and VSWR

Frequency (MHz)	Input impedance (Ω)		VSWR	Reflection coefficient (dB)
	R	X		
460	29.0907	j0.567951	1.71909	-11.5527
1262	70.5434	-j 0.05527	1.410869	-15.36931

Table (4) The gain of the proposed antenna at the resonant frequencies in the two planes

F(MHz)	Gain (dBi)	
	XZ-plane (phi=0°)	YZ-plane (phi=90°)
460	2.03	1.88
1262	1.62	4.45

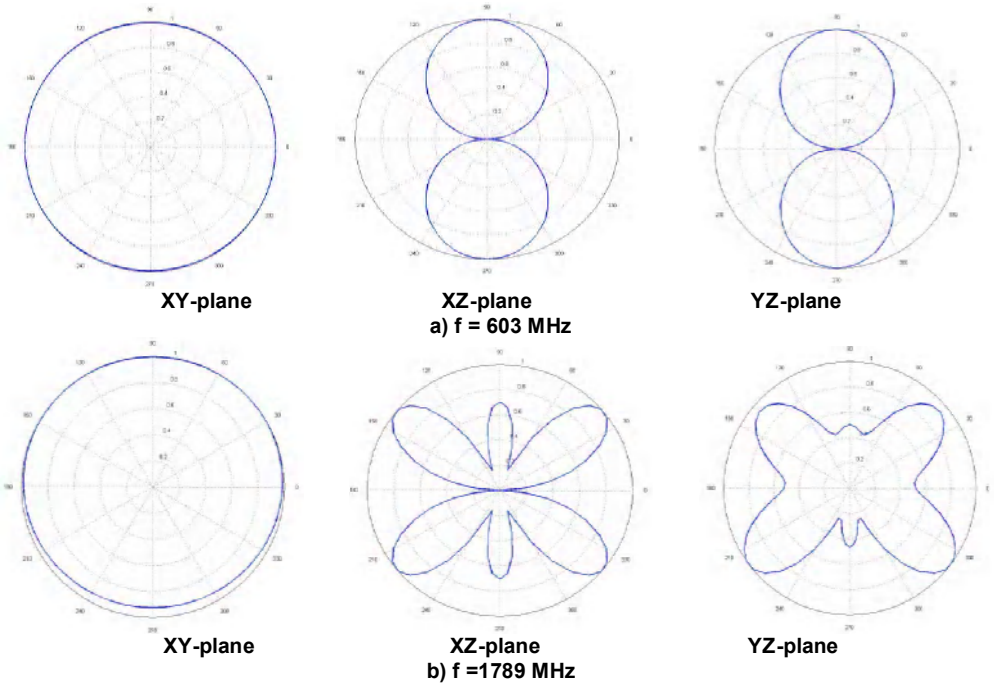

Fig. (7) Normalized electric field pattern at (a) f = 603MHz (b) f = 1789MHz

The antenna reflection coefficient with respect to 50Ω transmission lines was plotted in Fig. (9) and the VSWR is plotted in Fig. (10). The Normalized Electric field patterns in the three planes (XY-plane, XZ-plane, and YZ-plane) are plotted in Fig. (11) for each resonant frequency which is 460MHz and 1262MHz, respectively.

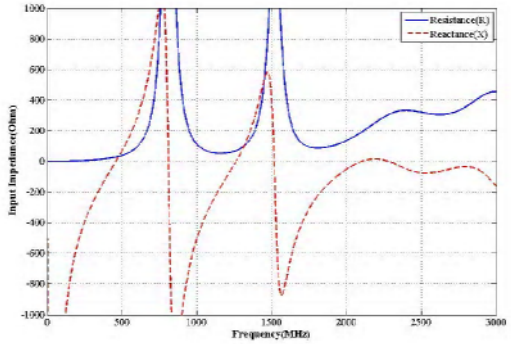

Fig. (8) Input impedance for the 1st iteration Quadratic Koch Curve

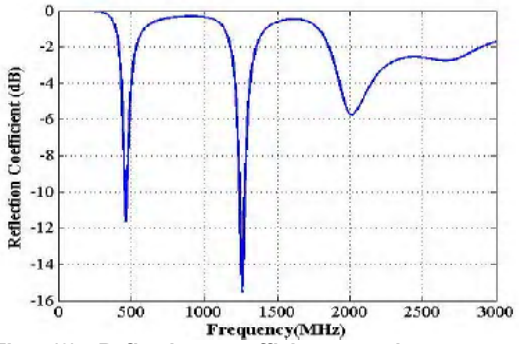

Fig. (9) Reflection coefficient at the antenna terminals

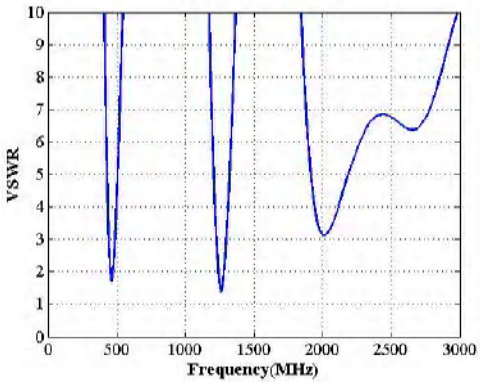

Fig. (10) Voltage-to-standing wave ratio (VSWR) at the antenna terminals

7. Conclusions

In this paper, multiple resonant frequencies of a fractal element antenna using triangular Koch curve and quadratic Koch curve was investigated, The results of the numerical studies, where Method of Moments was used to explore the behavior of the Koch fractal elements. The analysis and simulations of 1st iteration Triangular and Quadratic Koch curve dipole antennas shows some important points. The using of Koch curves in antenna design can help to design antennas with length smaller than the normal dipole and radiate with characteristics comparable to this $\lambda/2$ dipole. The simulations of triangular Koch curve and quadratic Koch curve dipole fractal antennas show that these antennas have their first resonance frequency below the design frequency, where for triangular and quadratic Koch curves dipole antenna the

percentage difference was 19.6% and 38.7%, respectively.

The fractal dimension (FD) for triangular Koch curve dipole antenna is equal to 1.2618, while for quadratic Koch curve dipole antenna is equal to 1.5. The reflection coefficient for the triangular Koch dipole antenna is <-10 dB (VSWR<2) at first resonance frequency and have small reactance equal to -j0.0376 for *f*=603MHz and -j0.442 for *f*=1789MHz.

The reflection coefficient for the quadratic Koch dipole antenna is <-10dB (VSWR<2) at each resonance frequency and have small reactance equal to j0.567951 for f=460MHz and -j0.05527 for f=1262MHz. The resistance of triangular and quadratic Koch dipole antenna at some resonance frequencies is not equal to 50Ω, only the first frequency of the triangular Koch dipole antenna approximately 50Ω. So, to obtain the resistance equal to 50Ω at all frequencies must using matching circuits.

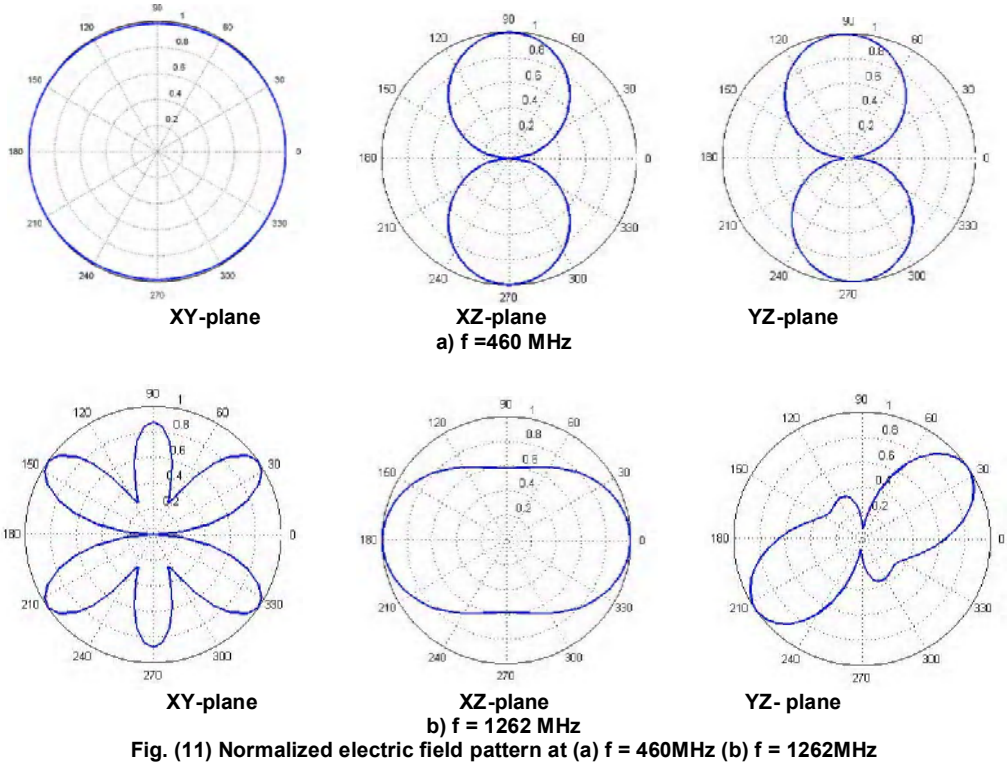

XY-plane XZ-plane YZ-plane

a) f =460 MHz

XY-plane XZ-plane YZ- plane

b) f = 1262 MHz

Fig. (11) Normalized electric field pattern at (a) f = 460MHz (b) f = 1262MHz

References

[1] X. Yang et al., *Appl. Microwave and Wireless,* 5(11) (1999) 34-46.

[2] K. Falconer, **"Fractal Geometry; Mathematical Foundations and Applications",** 2nd ed., John-Wiley & Sons Ltd. (2003).

[3] J. Gianvittorio, "Fractal Antennas: Design, Characterization and Applications", M.Sc. thesis. University of California, Los Angeles, (2000).

[4] D. Werner and S. Ganguly, *IEEE Antennas and Propagation Magazine*, 45(1) (2003) 38-56.

[5] V. Rusu et al., "Fractal Antennas", Bucharest University, *private communications.*

[6] "Why Fractal Shape antennas", available at www-tsc.upc.es/eef/research_lines/Antennas/fractals/history.html#classics

[7] P.S. Addison, "**Fractals and Chaos**", IOP Publishing, Institute of Physics (London), Ch. 2 (1997) 8-26.

IMCIC 2010

The International Multi-Conference on Complexity, Informatics and Cybernetics

April 6-9, 2010 - Orlando, FL, USA

http://www.2010iiisconferences.org/IMCIC

The deadlines are the following:
Papers/Abstracts Submissions and Invited Sessions Proposals:

October 21st 2009

Authors Notifications:

November 16th 2009

Camera-ready, full papers:

December 16th 2009

All Submitted papers/abstracts will go through three reviewing processes: (1) double-blind (at least three reviewers), (2) non-blind, and (3) participative peer reviews. These three kinds of review will support the selection process of those papers/abstracts that will be accepted for their presentation at the conference, as well as those to be selected for their publication in JSCI Journal.

Pre-Conference and Post-conference Virtual sessions (via electronic forums) will be held for each session included in the conference program, so that sessions papers can be read before the conference, and authors presenting at the same session can interact during one week before and after the conference. Authors can also participate in peer-to-peer reviewing in virtual sessions.

Submissions for Face-to-Face or for Virtual Participation are both accepted. Both kinds of submissions will have the same reviewing process and the accepted papers will be included in the same proceedings.

Authors of accepted papers who registered in the conference can have access to the evaluations and possible feedback provided by the reviewers who recommended the acceptance of their papers/abstracts, so they can accordingly improve the final version of their papers. Non-registered authors will not have access to the reviews of their respective submissions.

Registration fees of an effective invited session organizer will be waived according to the policy described in the web page (click on 'Invited Session', then on 'Benefits for the Organizers of Invited Sessions'), where you can get information about the ten benefits for an invited session organizer. For Invited Sessions Proposals, please visit the conference web site, or directly to

http://www.2010iiisconferences.org/imcic/organizer.asp

Authors of the best 10%-20% of the papers presented at the conference (included those virtually presented) will be invited to adapt their papers for their publication in the Journal of Systemics, Cybernetics and Informatics.

IMCIC 2010

Mario Wilson[1]
Mario Huicochea[2]

[1]*Center for Research in Optics, Loma del Bosque 115, Col. Campestre, Leon Gto, 37150, Mexico*
[2]*Center for Research in Mathematics, Jalisco s/n, Col. Valenciana, Guanajuato, Gto., 36240, Mexico*

Duffing Chaotic Laser Resonator

In this work we show, from the dynamical point of view, how an optical device in a ring resonator can generate a Duffing map for the ray parameters. The resonator is analyzed and the elements of the matrix [a, b, c, e] representing the chaos generating device are found in terms of both, the cavity and the Duffing map parameters. The recurrence relations of the chaotic Duffing map are used to obtain the expressions that describe the ray after the n-th round trip. The characteristic dynamics of the Duffing chaos generating element are discussed and the matrix elements [a, b, c, e] of the chaos generator device are presented.

Keywords: Chaos, Duffing, Resonator
Received: 27 August 2009, **Revised**: 1 October 2009, **Accepted**: 8 October 2009

1. Introduction

Any system in nature let it be optical, chemical, mechanical electrical or even economical [1, 2] can exhibit chaotic behavior. In the last decades, scientists have studied chaotic physical systems in search of good theoretical or computational models to describe them, conversely, their theoretical and computational studies of chaos has often stimulated the search for physical systems that would behave according to a model predictions. In this work it is shown that the dynamics of a light beam in a laser resonator with a chaos generating optical device within may be made to follow Duffing set of equations [3]. The conditions imposed on the optical device for the beam to obey Duffing equations are discussed [4, 5, 6, 7]. Most of the research on chaotic systems has concentrated on their temporal behavior [8, 9, 10, 11]; this work is focused on the spatial behavior of a ray in a laser cavity. The idea behind this work is to make the variables involved in the matrix laser function like in an oscillating Duffing pendulum [12].

2. Duffing Map

The Duffing oscillator is a non-linear system; it is a good example of a periodic forced oscillator with a non linear elasticity, it can exhibit both a periodic and a chaotic response. As an undamped driven oscillator, Duffing is described as a second order differential equation:

$$\ddot{x} + \alpha\dot{x} + x + x^3 = \beta\cos\omega t \qquad (1)$$

When studied in phase space, this equation gives rise to the Duffing map [13], best described by a difference equations system:

$$\begin{cases} \dfrac{dx}{dt} = z \\ \dfrac{dz}{dt} = -x - x^3 - \alpha z + \beta\cos(\omega t) \end{cases} \qquad (2)$$

In paraxial optics, two parameters are of importance: $y_n, (z)$ for the effective distance to the optical axis z and $\theta_n\,(z)$ the angle to the same axis, the subscript n designs the n^{th} ray's complete trip; so that when a two-dimensional non-linear map in its discrete form is applied to a paraxial ray in a laser cavity, the Duffing equations can be written as follows:

$$\begin{cases} y_{n+1} = \theta_n \\ \theta_{n+1} = -\beta * y_n + \alpha * \theta_n - \theta_n^3 \end{cases} \qquad (3)$$

The Duffing map written as in equation (3) describes the transformation a ray (y_n,, θ_n) undergoes in one round trip inside the laser cavity, and reveals the new point (y_{n+1}, θ_{n+1}).

This map depends on the two parameters "α" and "β", usually set to α=0.25 and β=0.3 if chaotic behavior is desired. The Duffing equations (2) are often used to describe the movement of a classic particle inside a potential [14]. Figure (1) shows the Duffing attractor with these particular values of α, β and ω=1, here a two well potential appears since there are two stable points.

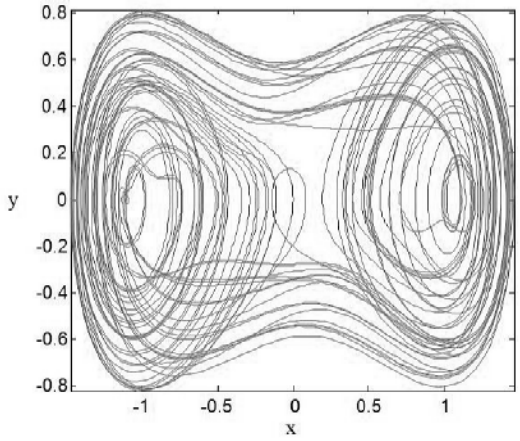

Fig. (1) Duffing chaotic attractor with parameters α=0.25, β= 0.3 and ω=1

To see the fixed points of the Duffing map θ_n is plotted as a function of n (for values of n from 0 to 800) in Fig. (2). The Duffing phase space is shown for the discrete expression in Fig. (3) for the same particular values of α and β; θ_n is plotted as function of y_n.

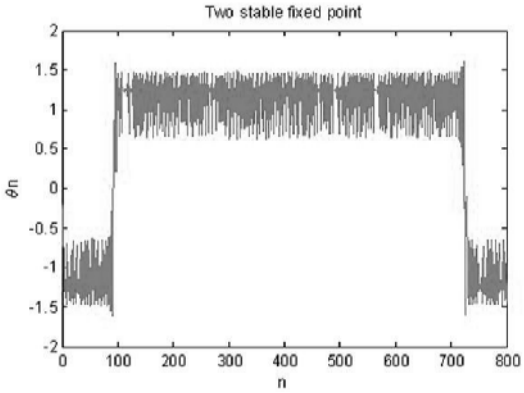

Fig. (2) The figure shows the two stable fixed points

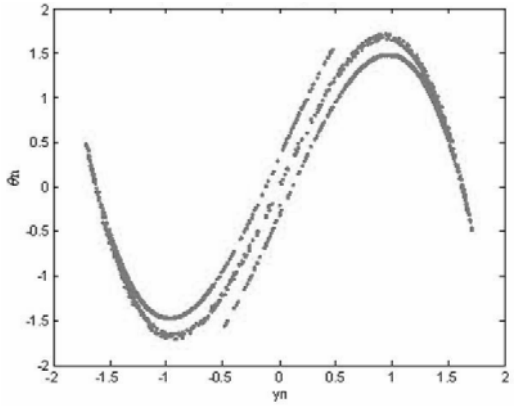

Fig. (3) Discrete-time Duffing map with α=0.25 and β=0.3

3. Resonator Optics

A laser cavity can, as any optical device, be described by an ABCD matrix or ray matrix. Such a matrix is a 2x2 matrix, originally developed for calculating the propagation of geometric rays with some transverse offset y and offset angle θ from a reference axis. As long as the angles involved are kept small (paraxial approximation), that is $\sin\theta \approx \tan\theta \approx \theta$, there is a linear relation between the y and θ coordinates before and after an optical element, and the transformation a light ray undergoes when passing through an optical element, can be expressed by the following equation:

$$\begin{pmatrix} y_2 \\ \theta_2 \end{pmatrix} = \begin{pmatrix} A & B \\ C & D \end{pmatrix} * \begin{pmatrix} y_1 \\ \theta_1 \end{pmatrix} \tag{4}$$

For any optical system, if a beam propagates through several optical elements (including any air spaces in between) it is always possible to obtain the system's total [A,B,C,D] matrix by taking the matrix product of each one of the optical elements in the system.

If a resonator formed by two plane mirrors and an ideal phase conjugated mirror [15-20] separated by a distance d as shown in Fig. (4), with in addition, an unknown chaos generating element represented by the matrix [a, b, c, e] located in the middle of the optical way between the plane mirrors at a distance (d-b)/2, is to be described by a single [A, B, C, D] matrix, the calculation would yield:

$$\begin{pmatrix} A & B \\ C & D \end{pmatrix} = \begin{pmatrix} 1 & 0 \\ 0 & -1 \end{pmatrix} \begin{pmatrix} 1 & d \\ 0 & 1 \end{pmatrix} \begin{pmatrix} 1 & 0 \\ 0 & 1 \end{pmatrix} \begin{pmatrix} 1 & \frac{d-b}{2} \\ 0 & 1 \end{pmatrix} \begin{pmatrix} a & b \\ c & e \end{pmatrix} \begin{pmatrix} 1 & \frac{d-b}{2} \\ 0 & 1 \end{pmatrix} \begin{pmatrix} 1 & 0 \\ 0 & 1 \end{pmatrix} \begin{pmatrix} 1 & d \\ 0 & 1 \end{pmatrix} \tag{5}$$

and the elements of the above total transformation matrix of the resonator would be:

$$A = a - \frac{c}{2}(b - 3d) \tag{6}$$

$$B = \frac{1}{4}(b^2 c - 2b(-2 + a + 3cd + e) + 3d(2a + 3cd + 2e)) \tag{7}$$

$$C = -c \tag{8}$$

$$D = \frac{bc - 3cd - 2e}{2} \tag{9}$$

Once we know the matrix of the system, we can carry out the calculations for the beam parameters $y(z)_n$ and $\theta(z)_n$ after n round trips. This will enable one to find the mathematical properties that the chaotic device has to fulfill.

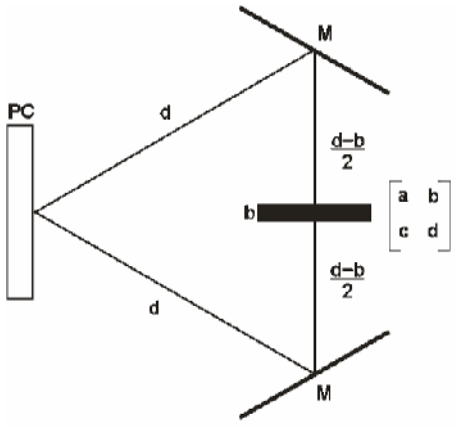

Fig. (4) Ring resonator constructed with two plane mirrors and one phase conjugated mirror including a chaos generating element

4. Duffing Chaos

Chaos and instabilities have been an area of research in simple lasers, and in 1991, some experimental work was done [21] in composite resonator lasers with a phase-conjugator mirror to demonstrate that the laser system behaves as a system of forced non linear oscillators, the authors reported that the attractor they found has the characteristics of the one obtained for the Duffing's equation.

The matrix [*a* ,*b, c, e*] of the chaos generating element needs to be found, so that equations (3) and (6), (7), (8), (9) form a consistent system. The matrix system (3) is equivalent to:

$$\begin{aligned} y_{n+1} &= Ay_n + B\theta_n, \\ \theta_{n+1} &= Cy_n + D\theta_n. \end{aligned} \tag{10}$$

If one wants to obtain the Duffing map equations (3) from equations system (10) inspection alone indicates that one has to impose the following values to the matrix elements,

$$\begin{aligned} &A = 0, \quad B = 1, \\ &C = -\beta, D = \alpha - \theta_n^2. \end{aligned} \tag{11}$$

So that equations (6), (7), (8) and (9) respectively can be written as the following system of equations

$$0 = a - \frac{c}{2}(b - 3d) \tag{12}$$

$$1 = \frac{1}{4}(b^2 c - 2b(-2 + a + 3cd + e) + 3d(2a + 3cd + 2e)) \tag{13}$$

$$\beta = c \tag{14}$$

$$\alpha - \theta^2 = \frac{bc - 3cd - 2e}{2} \tag{15}$$

When the system of equation for elements *a, b, c* and *e* is solved, the results are:

$$a = \frac{2 + \alpha - \theta^2 - \sqrt{\alpha^2 + 4\beta(-1 + 3d) - 2\alpha(-2 + \theta^2) + (-2 + \theta^2)^2}}{2} \tag{16}$$

$$b = \frac{2 + \alpha + 3\beta d - \theta^2 - \sqrt{\alpha^2 + 4\beta(-1 + 3d) - 2\alpha(-2 + \theta^2) + (-2 + \theta^2)^2}}{\beta} \tag{17}$$

$$c = \beta \tag{18}$$

$$e = \frac{2 - \alpha + \theta^2 + \sqrt{\alpha^2 + 4\beta(-1 + 3d) - 2\alpha(-2 + \theta^2) + (-2 + \theta^2)^2}}{2} \tag{19}$$

Taking the solutions (16) to (19) for the elements of the matrix [*a*, *b*, *c*, *e*] into Eq. (5), the total transformation matrix [*A*, *B*, *C*, *D*] for a full round trip is governed by the elements given by equations system (3). Now equations for y_{n+1} and θ_{n+1} are readily obtained and by construction will have a Duffing system form that will only depend on the parameters α, β and *d*. This means that the chaos generating device lead the laser system to any behavioral region (one potential well or two) determined by α and β.

5. Conclusions

This work shows that it is possible to model a chaos generating element capable of modifying the lasers dynamics; particularly, a Duffing pendulum system behavior was induced. The laser resonator that we proposed is a ring resonator formed by two plane mirrors and a phase conjugated mirror with a an optical device between the two plane mirrors, Chaos is obtained in the spatial domain, in terms the laser spot size and in the angle of the ray with the optical axis, and is described by the system equation (16) to (19). In this particular case, a dependence of the Duffing chaos generating element with the distance between the mirrors can be clearly observed. The elements of the matrix for the Duffing chaos generating element [*a*, *b*, *c*, *e*] are found in this work for the first time to our knowledge and was used to lead the laser behavior as a Duffing pendulum system.

References

[1] C.K. Yolasi, I.M. Kyprianidisi and I.N. Stovboulosi, J. of Istanbul Kültür Univ. (2006).

[2] V. Aboites, in *Handbook of Optical Engineering,* ed. Marcel Dekker (NY) (1999) 719-734.

[3] A.H. Nayfeh, ***"Introduction to Perturbation Techniques"***, John-Wiley & Sons (NY) (1993).

[4] B. Lü and L. Pan, *Opt. Comm.*, 205 (2002) 7-16.

[5] C. Gamachl, et. al., *Science,* 280 (1998) 1556.

[6] V. Aboites, *Dynamics of a laser resonator*, IJPAM, 36(4) (2007) 345-352.

[7] V. Aboites, M. Wilson, *Tinkerbell Chaos in a ring phase-conjugated resonator*, IJPAM, 54(3) (2009) 429-435.

[8] H. Meng et al., *Rev. Mex. Fis.*, 36(3) (1990) 335.
[9] H. Meng et al., *Rev. Mex. Fis.*, 38(3) (1992) 427.
[10] V. Aboites, *Int. J. Bifur. & Chaos*, 18(6) (2008) 1821-1824.
[11] P.J. Soan et al., *Optics Lett.*, 19(11) (1994) 783.
[12] G. Duffing, *Erzwungene Schwingungen bei Veränderlicher Eigenfrequenz*., F. Vieweg u. Sohn, Braunschweig, (1918).
[13] F. Pappof, et. al., *Phys. Rev. Lett.*, 68(8) (1992) 1128-1131.
[14] H. Peitgen, H. Jürgens and D. Saupe, *Chaos and Fractals. New Frontiers of Science*, 2nd ed., Springer (2004).
[15] V. Aboites, *Rev. Mex. Fis.*, 37(3) (1990) 391.
[16] V. Aboites and A. Kiryanov, *Phase Conjugated Lasers*, *Some Topics of Modern Optics*, ed. Rodriguez-Vera and Mendoza-Santoyo, Rinton Press, U.S.A. (2008).
[17] B. Barrientos et. al., *J. of Optics*, 26(3) (1995) 97.
[18] B. Barrientos et. al., *Appl. Opt.*, 35(27) (1996) 5386.
[19] A. Kiryanov et al., *J. Opt. Soc. Amer.*, B17(1) (2000) 11.
[20] E. Rosas et al., *Opt. Commun.*, 174 (2000) 243.
[21] C.Yongxing, et. al., *Chinese Phys. Lett.*, 8(11) (1991) 559.

Temperature Dependency of Hall Coefficients in Cadmium Oxide Thin Films Prepared by Thermal Evaporation Technique

Haitham M. Mikhlif
Asmaa M. Raouf
Asmaa D. Nusaif

Department of Physics,
College of Science,
Al-Mustansiriya University,
Baghdad, Iraq

In this work, the temperature dependencies of Hall coefficients in cadmium oxide thin films prepared by thermal evaporation technique. These coefficients included temperature-dependent Hall coefficient, logarithmic Hall coefficient and Hall mobility. Results showed that the extrinsic conduction prevails in studied samples and impurity atoms introduce energy levels within the energy gap and act as donors. The activation energy of the impurities generally ranged between 0.020eV and 0.070eV. An increase of carrier mobility with temperature was observed then it decreased in higher temperature due to lattice scattering of charge carriers. The values of optical bandgap ranged between 2.90eV and 3.30eV, which is in a good agreement with the those obtained for bulk CdO:Sn samples.

Keywords: CdO films, Hall coefficients, Temperature dependency, Thermal evaporation
Received: 11 July 2009, **Revised**: 22 September 2009, **Accepted**: 5 October 2009

1. Introduction

Degenerate semiconducting cadmium oxide (CdO) material attracts a great attention due to its electrical and optical properties. Films prepared from pure and metal-doped CdO have been widely studied for extensive optoelectronic applications in transparent conducting oxides (TCO), solar cells, smart windows, optical communications, flat panel displays, photo-transistors, as well as other types of applications like IR heat mirror, gas sensors, low-emissive windows, thin-film resistors, etc [1–5].

Generally, CdO films are transparent in visible and NIR spectral regions and have n-type semiconducting properties with an electrical resistivity of 10^{-2}–10^{-4} Ω.cm [1, 6] and a band gap in-between 2.2eV and 2.7eV [7–9]. The procedure of preparation and the kind of the metal dopant are responsible for those different values of the conductivity and the variety of the optical properties. The conduction of pure CdO is attributed to its native defects of oxygen vacancies and cadmium interstitials. Therefore, the conductivity of CdO films can be controlled by those native defects through the procedure of film preparation including doping with metallic ions. Moreover, these electrical properties can be improved by reducing the effect of depletion regions formed on grain boundaries that can be done by employing various treatments with hydrogen including low-temperature post-annealings [10–12]. The present study focuses on the improvement of the dc-electrical conduction properties and the variation in the optical absorption properties of CdO thin films because of low-temperature post-annealing in hydrogen atmosphere at different durations.

Cadmium oxide (CdO) is an important semiconductor material for the development of various technologies of solid–state devices, (panel display, optoelectronic components, thermally insulating glass, etc.) [7,13,14]. Some electrical properties of this oxide have been investigated by several authors [9,15-17]. The experimental data concerning the Hall effect of CdO are rather poor. A variety of methods has been used to prepare thin films of cadmium oxide such as thermal evaporation, oxidation of cadmium films, spray pyrolysis, metalorganic chemical deposition, etc. [9,16-18]. It was experimentally found that the electronic transport and optical properties of CdO thin films strongly depend on the preparation method and deposition conditions [1618]. On the other hand, we remark, that in the above-mentioned papers on the electronic transport in CdO and CdO:Sn thin films, the experimental data were discussed with respect to a relative, small number of samples prepared under different conditions. Consequently, it is difficult to compare the results presented by different authors. In a series of previous papers [19-20], we have studied temperature dependence of the electrical conductivity of CdO and CdO:Sn thin films. It was experimentally established that the stable structure of films can be obtained if, after preparation, they are submitted to a heat treatment.

In present paper, the Hall coefficient in CdO:Sn thin films are investigated as a function of deposition conditions, magnetic induction and film temperature.

2. Experiment

CdO thin films were deposited onto glass substrates by physical vapor deposition under vacuum of high purity CdO. The experimental conditions were settled for obtaining films of a uniform thickness on large areas of the substrate surface. The samples under study were prepared using the following deposition parameters: the source evaporator-substrate distance was D=50mm; source temperature was T_v=1100K; deposition rate was r_d=10Å/s; substrate temperature T_S=300-500K. Source temperature was monitored by a Pt/Pt-Rh thermocouple. A special holder for substrates was made of aluminium and permits to prepare four samples simultaneously. A chromel-alumel thermocouple, which monitored substrate temperature, was attached to the front surface of the substrate. The film thickness was measured by using multiple-beam Fizeau's fringe method [22] at reflection of monochromatic light, λ=550nm.

For measurement of the Hall coefficient and its temperature dependence a special arrangement has been used [19,20]. The indium thin film electrodes were used. The Hall voltage was determined by a standard DC potentiometric method. Two Keithley instruments (Model 6517 electrometer) were used for measurements. The Hall coefficient was calculated from the following expression [23]

$$R = \frac{U_H d}{BI} \qquad (1)$$

where U_H is Hall voltage, d is film thickness, B is magnetic induction and I is intensity of total current which passes through the film

The magnetic induction produced by an electromagnet was measured by a teslameter. The temperature dependence of the electrical conductivity (σ) was studied using surface-type cells. The optical bandgap of CdO thin films was determined from optical absorption spectra. The absorption coefficient (α) was calculated from the expression [24]

$$\alpha = \frac{1}{d}\ln\frac{(1-R)^2}{T} \qquad (2)$$

where d is film thickness, and R is reflection coefficient and T is transmission coefficient

3. Results and Discussion

The temperature dependence of the Hall coefficient is presented in Figs. (1) and (2). An exponential decrease of Hall coefficient with increasing temperature is observed in all investigated temperature range. Clearly, the extrinsic conduction prevails in studied samples. Impurity atoms (tin atoms) introduce energy levels within the energy gap and act as donors. The activation energy of the impurities, E_d, calculated from the dependences $\ln(R_H T^{3/2}) = f(10^3/T)$ [23], generally ranged between 0.020eV and 0.070eV.

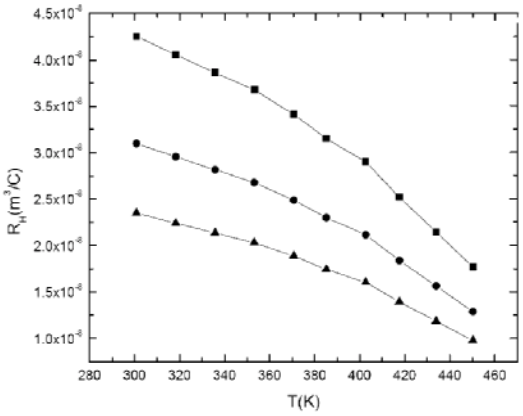

Fig. (1) Temperature dependence of the Hall coefficient for films with various thickness

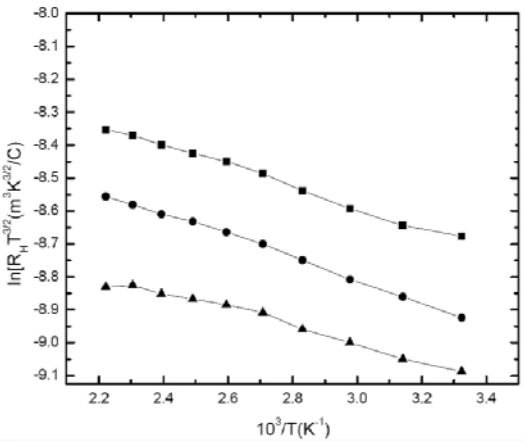

Fig. (2) Temperature dependence of the Hall coefficient for films with various thickness

In Fig. (3), the dependence of the Hall mobility on the temperature is illustrated for three samples. The Hall mobility (μ_H) has been estimated by means of the expression

$$\mu_H = \frac{|R_H|}{\rho} \qquad (4)$$

where R_H is Hall coefficient and ρ is the electrical resistivity

It is known that carrier mobilities depend on the predominant scattering mechanism in studied sample. In bulk semiconductors two scattering mechanisms are dominant: the scattering of the carriers by crystal lattice and scattering by ionized impurities. The carrier mobility due to lattice vibrations can be expressed by [25]

$$\mu_L = \frac{A_L}{\sqrt{m_{eff}^5 T^3}} \qquad (5)$$

and charged ionized centers affect mobility as follows [25].

$$\mu_I = \frac{A_I}{\sqrt{m_{eff} T^3}} \quad (6)$$

where A_L and A_I are the characteristic parameters, m_{eff} is effective mass of charge carriers and T is absolute temperature

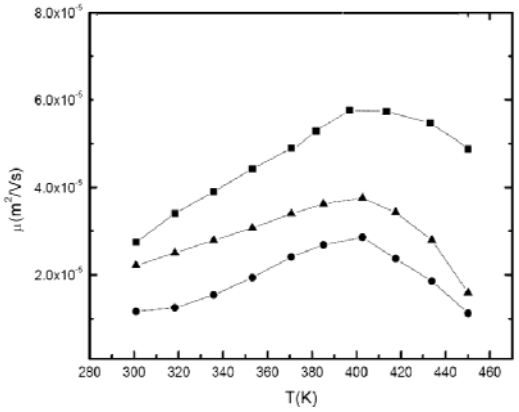

Fig. (3) Temperature dependence of the Hall mobility for films with various thickness

In the polycrystalline thin films, free carriers are scattered by the crystallite boundary surface in addition to the scattering mechanisms observed in respective bulk materials. It can be observed that these dependences present two parts. We suppose that in the first part the carrier scattering by ionized impurities (tin donors) prevails. According to Eq. (6), in this case an increase of carrier mobility with temperature is observed. The decrease of mobility in higher temperature is caused by lattice scattering of charge carriers. Also, the large value of the carrier concentration determines a decrease of the mobility [25].

By studying transmission and absorption spectra of CdO thin films, very useful information can be obtained about the energy gap, position of impurity levels in forbidden band, characteristics of optical transitions, etc. For investigated samples, the values of optical energy band gap have been calculated using absorption spectra. The determination of E_g from the absorption spectra seems to be more appropriate. An important characteristic of absorption spectra for polycrystalline semiconducting films is an additional maximum (compared to single crystals) for photon energies less than band gap.

At higher photon energy the absorption spectra are little influenced by polycrystalline structure of the films. For allowed direct band-to-band transitions (neglecting exciton effects), the energy dependence of absorption coefficient, a, near the band edge, is given by [24]

$$\alpha = \frac{Aa}{h\nu}\sqrt{h\nu - E_g} \quad (7)$$

where $h\nu$ is the photon energy and Aa is the characteristic parameter (independent to photon energy) for respective transitions

According to Eq. (7), the $(\alpha h\nu)^2 = f(h\nu)$ dependences are linear. Consequently, the optical band gap, (E_{g0}), can be determined by extrapolating the linear portions of mentioned dependences to $(\alpha h\nu)^2 = 0$.

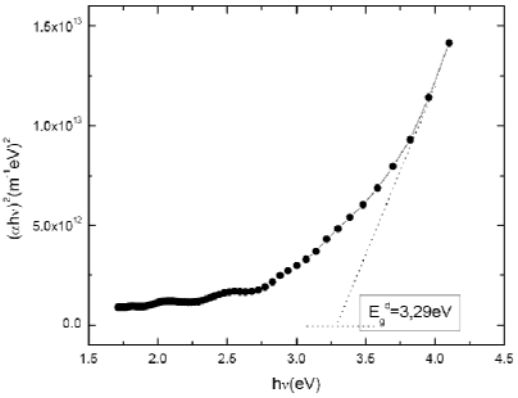

Fig. (4) Absorption spectra for CdO:Sn thin films

A typical absorption spectrum is presented in Fig. (4). For studied samples, the values of E_{g0} ranged between 2.90eV and 3.30eV, which is in a good agreement with the E_{g0} values obtained for bulk CdO:Sn samples.

4. Conclusion

In conclusion remarks, the extrinsic conduction prevails in studied samples and impurity atoms introduce energy levels within the energy gap and act as donors. The activation energy of the impurities generally ranged between 0.020eV and 0.070eV. An increase of carrier mobility with temperature was observed then it decreased in higher temperature due to lattice scattering of charge carriers. The values of optical bandgap ranged between 2.90eV and 3.30eV, which is in a good agreement with the those obtained for bulk CdO:Sn samples.

References

[1] Z. Zhao, D.L. Morel and C.S. Ferekides, *Thin Solid Films,* 413 (2002) 203.
[2] L.M. Su, N. Grote and F. Schmitt, *Electron. Lett.*, 20 (1984) 716.
[3] O. Gomez Daza et al., *Mod. Phys. Lett.*, B 17 (2001) 609.
[4] B.J. Lewis and D.C. Paine, *Mater. Res. Soc. Bull.*, 25 (2000) 22.
[5] M. Yan et al., *Appl. Phys. Lett.*, 78 (2001) 02342.
[6] D.M. Carballeda-Galicia et al., *Thin Solid Films*, 371 (2000) 105.

[7] K.L. Chopra and S.R. Das, **"Thin Film Solar Cells"**, Plenum Press (NY) (1993).
[8] Y.S. Choi, C.G. Lee and S.M. Cho, *Thin Solid Films*, 289 (1996) 0153.
[9] R. Kondo, H. Okhimura and Y. Sakai Y, *Japan. J. Appl. Phys.*, 10 (1971) 1547.
[10] K. Zhang et al., *J. Appl. Phys.*, 86 (1999) 974.
[11] S.Y. Myong and K.S. Lim, *Appl. Phys. Lett.*, 92 (2003) 3026.
[12] B.Y. Oh et al., *J. Cryst. Growth*, 281 (2005) 475.
[13] N. Tsuda, K. Nasu, A. Fujimori and K. Siratori, **"Electronic Conduction in Oxides"**, Springer-Verlag Berlin-Heidelberg-New York (2000).
[14] L.I. Maissel and R. Glang, **"Handbook of Thin Films Technology"**, McGraw-Hill (NY) (1970).
[15] C.H. Champness and C.H. Chan, *Sol. Energy Mater. Sol. Cells*, 37 (1995) 75.
[16] B.J. Lokhande and M.D. Uplane, *Mater. Res. Bull.,* 36 (2001) 439.
[17] A.A. Dakhel and F.Z. Henari, *Cryst. Res. And Technol.,* 38 (2003) 979.
[18] H. Metin and R. Esen, *Semicond. Sci. Tehnol.*, 18 (2003) 647.
[19] R.S. Rusu and G.I. Rusu, On the Electrical and Optical Properties of Polycrystalline CdO Thin Films, 7th Intern. Conf. Phys. Adv. Mater., 10-12 June 2004 Iassy-Romania.
[20] R.S. Rusu and G.I. Rusu GI, On the Hall Effect in CdO Thin Films, Workshop Fundam. Appl. Res. Phys., 3 November 2004, Iassy-Romania.
[21] M. Rusu, I. Nicolaescu and G. Rusu, *Appl. Phys.*, A70 (2000) 565.
[22] K.L. Chopra, **"Thin Film Phenomena"**, McGraw Hill (NY) (1969).
[23] E.H. Putley, **"The Hall Effect and Semiconductor Physics"**, Dover Publications (NY) (1969).
[24] O. Heavens, **"Optical Properties of Thin Solid Films"**, Dover Publications (NY) (1956).
[25] H.F. Wolf, **"Semiconductors"**, Wiley (NY) (1971).

Analytical Treatment to Minimize the Aberration in Concentric Lenses Employed in High-Power Irradiation Applications

Noor E.N. Alrawi
Jabbar A. Olaiwi

School of Applied sciences, University of Technology, Baghdad, Iraq

In this work, an analytical treatment to minimize the aberration (especially spherical) in concentric lenses was presented. The lenses concerned in this treatment are supposed to be graded-indexed optical elements of homogeneous surfaces. Spherical aberration is, contradictive to other types of aberrations, found possible to be eliminated in such optical elements as it is highly interested in high-power irradiation applications like laser-plasma interaction, microfabrication and fine-scaled metrology.

Keywords: Spherical aberration, Graded-indexed lenses, Optical design
Received: 20 July 2009, **Revised**: 22 September 2009, **Accepted**: 27 September 2009

1. Introduction

Lenses with spherical surfaces suffer spherical aberration and will cause problems when image resolution is required. One way to eliminate spherical aberration is to use gradient-indexed lenses [1-4]. Lenses with gradient refractive indices have also been manufactured successfully [5]. We have designed a new method to make what we call concentric gradient-indexed lenses [6], which use gradient-indexed spherical shells materials. When we let the object point right at the center of these spherical shells, we can make the light ray go straight into the lenses, and bend only when it goes out of the second surface to the image point, as shown in Fig. 1. Since the refractive indices at the bending surface of different radial distances have different values, we can choose the suitable refractive index gradient to eliminate the primary spherical aberration. We have also made some suggestions for the manufacture of concentric gradient-indexed materials [6]. One suggestion is to use non-equilibrium condensation of solid solutions, which are frequently found in Nature to form cored crystals but have not been massively used in the manufacture of lens materials. The cored phenomena indicate that the first condensed central part of the crystal has different composition from those condensed at the outer part, so that the refractive indices variations occur between inner and outer shells of crystals [7].

In this paper, we first derive all of the concentric gradient-indexed lenses and find a unified formulation, which is listed with a specific sign convention. Next, we find the Abbe points from these formulations. We also find, from these formulations, the spherical aberration tendency of homogeneous spherical surface lenses, which may help to reduce spherical aberration in the design of normal spherical surface lenses systems. Finally, we suggest some applications of concentric gradient-indexed lenses to microscope objective, and others.

2. Mathematical Treatment

We derive all of the cases in Fig. (1). The derivation methods to eliminate the primary spherical aberration are similar to that described elsewhere [6]. All of the cases are found to have the same result. If we set the refractive indices to be:

$$n(x) = n_0 - \Delta n(x) \tag{1}$$

then by the derivation method similar to that in a preliminary report [6], we can obtain:

$$\Delta n(x) = x n_0 \times \left(\frac{1}{L_1} - \frac{n_0}{L_2} \right) \tag{2}$$

where x is the axial coordinate with the origin at the central point of the lens upper surface, n_0 is the refractive index at the central point of the lens upper surface, the R in Fig. (1) is the radius of curvature of the lens upper surface, L_1 and L_2 are the object and image distances measured from the central point of the lens upper surface, respectively. The sign convention is different from that in previous work [6]. It is almost inevitable in geometrical optics that the sign convention suitable for derivation is not the same as that for application. In this paper, we set each and every positive x direction in the upper direction, as seen in Fig. (1). The real object is in the negative direction, so L_1, the object distance, is negative in the real object cases. The real image is in the positive direction, so L_2, the

image distance, is positive in the real image cases. The virtual object and virtual image cases have the opposite signs, positive for virtual objects and negative for virtual images. In Fig. (1), *H* means high refractive index, and *L* means low refractive index, which can be interpreted by Eqs. (1) and (2) for the various cases. The derivations to Eq. (2) must fulfill some approximations. For example, in the Fig. (1a) case [6],

$$\frac{|L_1|}{L_2}\times\frac{|x|}{|L_1|-|R|}<<1$$

$$\frac{x}{L_1}<<1$$

and others. We may say that the concentric gradient-indexed lenses have eliminated the primary spherical aberration, but not the higher order spherical aberration [2,6].

3. Results and Discussion

When we apply Eq. (2) to Figs. (1a) and (1f), we find that when $|L_2|=n_0|L_1|$ and L_1, L_2 with the same sign, all positive in Fig. (1f) or all negative in Fig. (1a), then $\Delta n_x=0$, that is, the medium is homogeneous and the primary spherical aberration is zero. These points are called Abbe points [2]. In fact, these points have no spherical aberration at all, which we do not prove here to save space.

The object points are at the centers of curvature of the first surfaces of the lenses. The lenses refractive indices are constant at each of the concentric spherical surfaces, but the refractive indices show gradient through different concentric spherical surfaces. The n_0 is the refractive index at the central point of the lens upper surface. The *x* axes point upward L_1 are the object distances measured from the central points of the lenses upper surfaces L_2 are the image distances measured from the central points of the lenses upper surfaces *H* means high refractive index, and *L* means low refractive index.

We can interpret from Eq. (2) and Fig. (1) that Abbe points are also the turning points of spherical aberrations of homogeneous spherical lenses. In Fig. (1a), by using Snell's law and paraxial approximation, we can find the relationship between L_1 and $|R|$. By Snell's law:

$$n_0\times\left(\frac{1}{|R|}+\frac{1}{L_1}\right)=\frac{1}{|R|}+\frac{1}{L_2} \qquad (3)$$

where n_0 is the refractive index at the central point of the lens upper surface, *R* is the radius of curvature of the lens upper surface, L_1 and L_2 are the object and image distances, respectively measured from the central point of the lens upper surface. Here we have used paraxial approximation and kept the sign convention in L_1 and L_2. By Eq. (2) we know that when $L_2=n_0L_1$ the lens refractive index gradient is zero; therefore the homogeneous lens will be free of spherical aberration. Substitute $L_2=n_0L_1$ to Eq. (3), and we get:

$$(n_0-1)\times\frac{1}{|R|}=\frac{1}{n_0L_1}-\frac{n_0}{L_1}=\left(\frac{1}{n_0}-n_0\right)\times\frac{1}{L_1} \qquad (4)$$

$$L_1=\frac{1-n_0^2}{n_0}\times\frac{|R|}{n_0-1}=-\frac{(n_0+1)\times|R|}{n_0} \qquad (5)$$

It can be verified that when the lens is homogeneous in Fig. (1a) and when $|L_1|>(n_0+1)|R|=n_0$ in Fig. (1a), then the off paraxial rays will intercept the optical axis backward to the paraxial image point. We may regard these as backward spherical aberrations. On the contrary, when $|L_1|<(n_0+1)|R|=n_0$, then the off paraxial rays will intercept the optical axis forward to the paraxial image point. We may regard these as forward spherical aberrations. The verification procedure is a bit tedious but may be worth listing for the sake of completeness. Rewrite Eq. (3) and we get:

$$\frac{L_1}{L_2}=L_1\times(n_0-1)\times\frac{1}{|R|}+n_0 \qquad (6)$$

When L_1 and L_2 are both negative, as in Fig. (1a), the increase of $|L_1|$ will cause ($L_1=L_2$) to become smaller. Therefore when $|L_1|>(n_0+1)|R|=n_0$, from Eq. (2) $\Delta n(x)$ will be negative for positive *x*, then by Eq. (1) we find the lens refractive index is up-high down-low, so that when the refractive index gradient disappears in a homogeneous lens condition, the off paraxial rays will bend harder than those rays corrected by down-low lenses, so the image point will be backward to the paraxial image point. Other cases can be verified in similar ways, but we will skip them to save space. In Fig. (1) cases the bending rays are penetrating from the high to the low refractive indices mediums. The opposite cases can be interpreted by reversing the ray directions in Fig. (1). We summarize in Fig. (2) the primary spherical aberration conditions when the light beams penetrating through two homogeneous mediums. These judgments can be used for homogeneous spherical lenses designs to reduce spherical aberration. For example, the combination of forward and backward cases can cancel each other out.

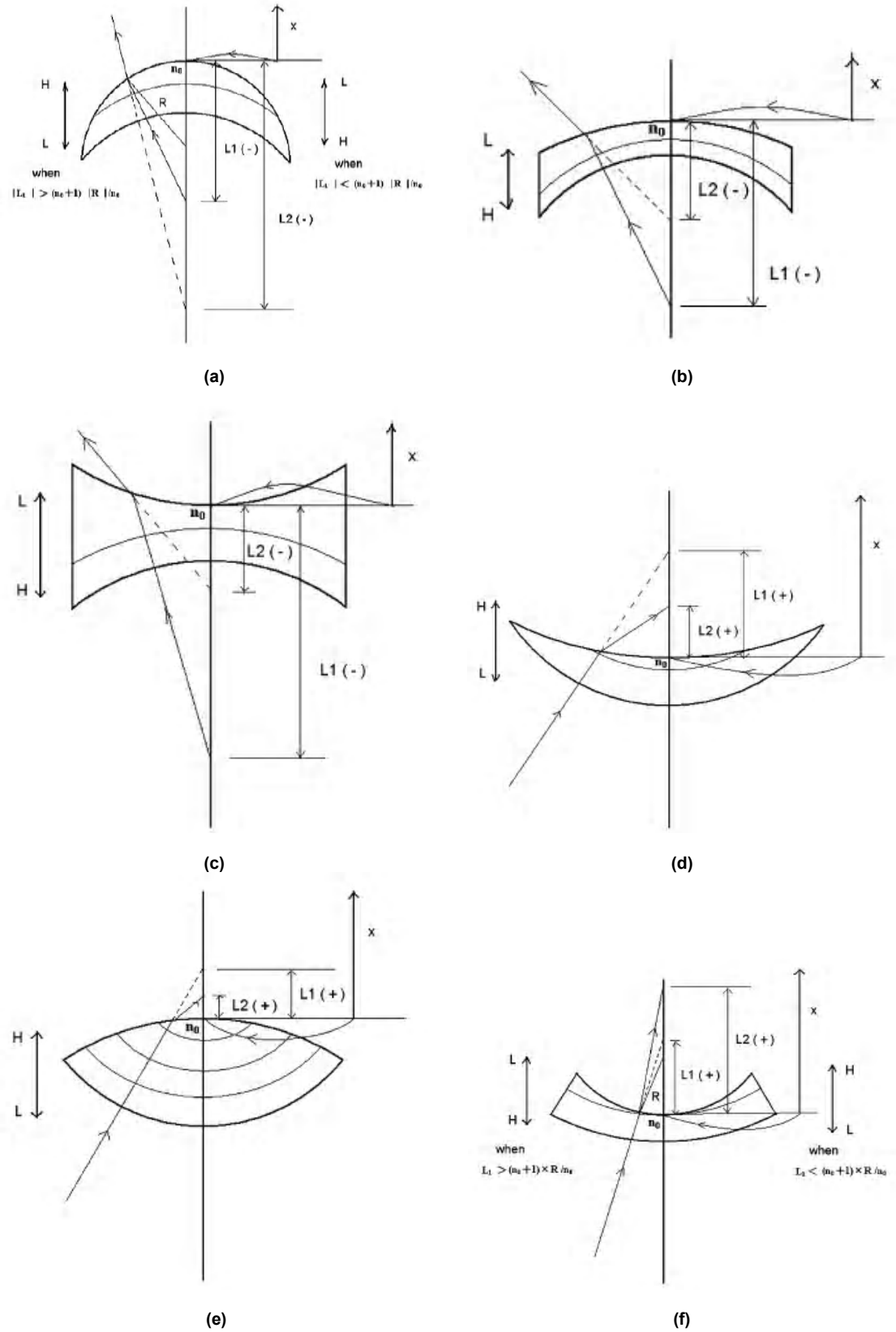

Fig. (1) Various concentric gradient-indexed lenses. (a) Concave-convex convex lens. (b) Concave-convex concave lens. (c) Bi-concave lens. (d) Convex-concave convex lens. (e) Bi-convex lens. (f) Convex-concave concave lens

In Fig. (2), **A** indicates the positions of Abbe points when the object points coincide with the Abbe points, they have no spherical aberration, while **B** indicates backward spherical aberrations; when the object points are in these ranges, the image points of the off-paraxial rays

ISSN 1813-2065

suffer backward spherical aberration, that is, to the left of the paraxial image points, and **F** indicates forward spherical aberrations; when the object points are in these ranges, the image points of the off-paraxial rays suffer forward spherical aberration, that is, to the right of the paraxial image points.

The lenses in Fig. (1) can be modified by having a flat surface either in the null surface or in the bending surface. The images in Figs. (1a) and (1f) can be real or virtual or at infinity, depending on the conditions. The ray direction may be reversed for all of the cases. These lenses may be used whenever good image quality is called for. For example, projection optics systems [9] used in the manufacture of integrated circuits and/or micro-electromechanical systems use many heavy lenses to get good image quality. The use of concentric gradient-indexed lenses may replace some lenses and/or reduce the number of lenses but still maintain good image quality. Projection optics lenses may need to be 50mm in diameter. It seems methods like the non-equilibrium condensation of solid solutions [6,7] are especially suitable for these big lenses, since the production procedures are similar to those for optical glass production. Certainly the try–investigation–error procedures are inevitable before the standard procedures for real productions may come true.

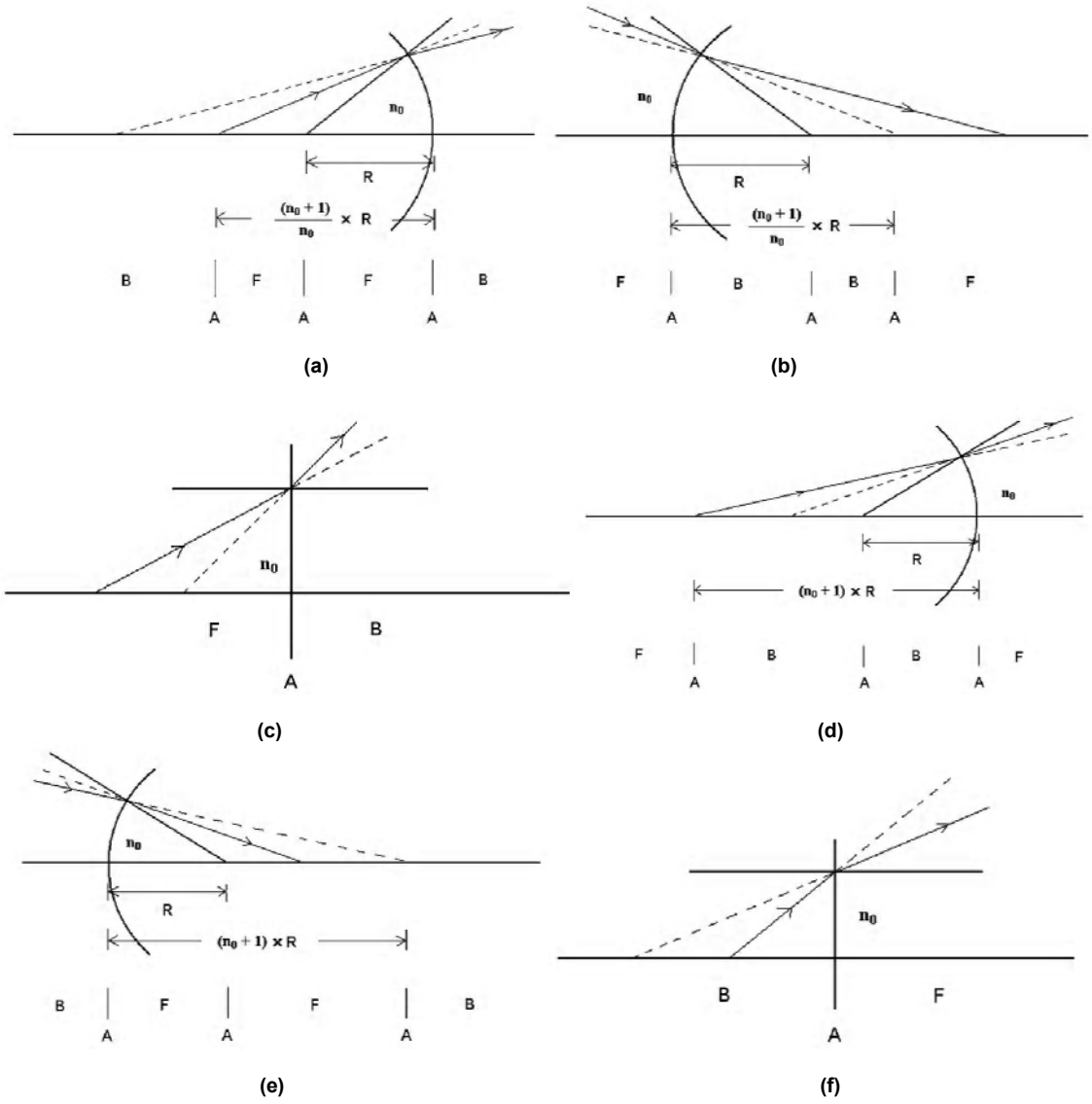

Fig. (2) Primary spherical aberrations caused by spherical interfaces. (a) High to low refractive index medium, facing concave surface. (b) High to low refractive index medium, facing convex surface. (c) High to low refractive index medium, facing flat surface. (d) Low to high refractive index medium, facing concave surface. (e) Low to high refractive index medium, facing convex surface. (f) Low to high refractive index medium, facing flat surface. n_0 is the relative refractive index of high to low refractive index medium. R is the radius of curvature of the spherical interface

4. Conclusions

We have found a unified formulation for all of the concentric gradient-indexed lenses and it can be used to find some Abbe points. We can also use the results to judge the longitudinal spherical aberrations of the spherical interfaces between two homogeneous mediums. The applications of the concentric gradient-indexed lenses are extremely found in microscope objective lenses and projection optics systems lenses for integrated circuits and the manufacture of micro-electromechanical systems.

References

[1] E.W. Marchand, **"Gradient Index Optics"**, Academic Press (New York, 1978).

[2] D. Malacara and Z. Maracara, **"Handbook of Optical Design"**, Marcel Dekker (New York, 2004).

[3] D.T. Moore, *J. Opt. Soc. Amer.*, 67 (1977) 1137.

[4] K. Kikuchi, S. Ishihara, H. Shimizu, and J. Shimada, *Appl. Opt.*, 19 (1980) 1076.

[5] H. Nishi, H. Ichikawa, M. Toyama, and I. Kitano, *Appl. Opt.*, 25 (1986) 3340.

[6] C.C. Lee, J. Hsu, and C.-H. Lee, *Jpn. J. Appl. Phys.*, 46 (2007) 7336.

[7] A.R. West, **"Basic Solid State Chemistry"**, Wiley (New York, 1999).

[8] M. Born and E. Wolf, **"Principles of Optics"**, Pergamon Press (Oxford, U.K., 1980).

[9] S. Franssila, **"Introduction to Microfabrication"**, Wiley (New York, 2004).

Iraqi Journal of Applied Physics
Subject Index 2005-2009

Quantum Physics & Spectroscopy

Semiconductors & Optoelectronics

Solid State Physics & Applications

* * *

* * *

ISSN 1813-2065

Iraqi Journal of Applied Physics
Author Index 2005-2009

K

L

M

N

O

P

R

S

T

U

V

W

Y

Z

ISSN 1813-2065

IRAQI JOURNAL OF APPLIED PHYSICS

CONTENTS